Cancer Cell

Article

Cancer immunotherapies transition endothelial cells into HEVs that generate TCF1$^+$ T lymphocyte niches through a feed-forward loop

Graphical abstract

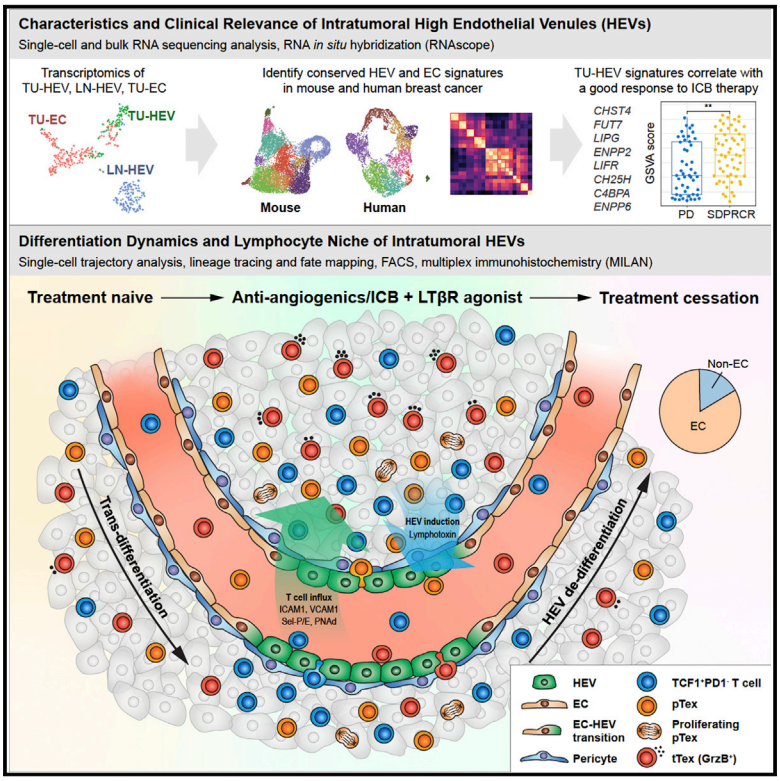

Highlights

- Tumor endothelial cells dynamically transition into high-endothelial venules (TU-HEVs)
- TU-HEVs require NK and CD8 T cell-derived signals for induction and maintenance
- TU-HEV niches enable PD1$^+$TCF1$^+$ progenitor CD8 T cell expansion into effector T cells
- The presence of a human HEV signature in tumors correlates with response to ICB therapy

Authors

Yichao Hua, Gerlanda Vella, Florian Rambow, ..., Jean-Christophe Marine, Susan Schlenner, Gabriele Bergers

Correspondence

gabriele.bergers@kuleuven.be

In brief

Hua et al. reveal that effective antiangiogenic immunotherapy differentiates postcapillary venules into high-endothelial venules (HEVs) by lymphotoxin beta receptor activation emanating from CD8 T and NK cell-derived signals. TU-HEVs establish perivascular niches in which TCF1$^+$PD1$^+$ lymphocytes expand and produce cytotoxic PD1$^+$TIM3$^+$ lymphocytes that may facilitate anti-tumoral immunity.

Hua et al., 2022, Cancer Cell *40*, 1600–1618
December 12, 2022
https://doi.org/10.1016/j.ccell.2022.11.002

CellPress

CellPress
OPEN ACCESS

Cancer Cell

Article

Cancer immunotherapies transition endothelial cells into HEVs that generate TCF1$^+$ T lymphocyte niches through a feed-forward loop

Yichao Hua,[1,2,3,20] Gerlanda Vella,[1,2,3,20] Florian Rambow,[1,3,4,5,6] Elizabeth Allen,[7] Asier Antoranz Martinez,[8] Marie Duhamel,[1,2,3] Akira Takeda,[9] Sirpa Jalkanen,[9] Steffie Junius,[10,11] Ann Smeets,[12] David Nittner,[1,13] Stefanie Dimmeler,[14] Thomas Hehlgans,[15] Adrian Liston,[11,16] Francesca Maria Bosisio,[8] Giuseppe Floris,[8] Damya Laoui,[17,18] Maija Hollmén,[9] Diether Lambrechts,[1,19] Pascal Merchiers,[7] Jean-Christophe Marine,[1,3,4] Susan Schlenner,[10] and Gabriele Bergers[1,2,3,21,*]

[1]VIB Center for Cancer Biology, Leuven, Belgium
[2]Laboratory of Tumor Microenvironment and Therapeutic Resistance, VIB Center for Cancer Biology, Leuven, Belgium
[3]Department of Oncology, KU Leuven, Leuven, Belgium
[4]Laboratory of Molecular Cancer Biology, VIB Center for Cancer Biology, Leuven, Belgium
[5]Department of Applied Computational Cancer Research, Institute for AI in Medicine, University Hospital Essen, Essen, Germany
[6]University of Duisburg-Essen, Essen, Germany
[7]Oncurious NV, Leuven, Belgium
[8]Department of Imaging & Pathology, Laboratory of Translational Cell & Tissue Research and Department of Pathology, University Hospitals Leuven, KU Leuven, Leuven, Belgium
[9]MediCity, Research Laboratory and InFLAMES Flagship, University of Turku, Turku, Finland
[10]Department of Microbiology, Immunology, and Transplantation, KU Leuven, Leuven, Belgium
[11]VIB Center for Brain and Disease Research, Leuven, Belgium
[12]Department of Surgical Oncology, University Hospitals Leuven, KU Leuven, Leuven, Belgium
[13]Department of Human Genetics, KU Leuven, Leuven, Belgium
[14]Institute of Cardiovascular Regeneration, Goethe-University, Frankfurt am Main, Germany
[15]Department of Immunology, University of Regensburg, Regensburg, Germany
[16]Laboratory of Lymphocyte Signalling and Development, The Babraham Institute, Cambridge, UK
[17]Laboratory of Dendritic Cell Biology and Cancer Immunotherapy, VIB Center for Inflammation Research, Brussels, Belgium
[18]Laboratory of Cellular and Molecular Immunology, Vrije Universiteit Brussel, Brussels, Belgium
[19]Laboratory for Translational Genetics, Department of Human Genetics, KU Leuven, Leuven, Belgium
[20]These authors contributed equally
[21]Lead contact
*Correspondence: gabriele.bergers@kuleuven.be
https://doi.org/10.1016/j.ccell.2022.11.002

SUMMARY

The lack of T cell infiltrates is a major obstacle to effective immunotherapy in cancer. Conversely, the formation of tumor-associated tertiary-lymphoid-like structures (TA-TLLSs), which are the local site of humoral and cellular immune responses against cancers, is associated with good prognosis, and they have recently been detected in immune checkpoint blockade (ICB)-responding patients. However, how these lymphoid aggregates develop remains poorly understood. By employing single-cell transcriptomics, endothelial fate mapping, and functional multiplex immune profiling, we demonstrate that antiangiogenic immune-modulating therapies evoke transdifferentiation of postcapillary venules into inflamed high-endothelial venules (HEVs) via lymphotoxin/lymphotoxin beta receptor (LT/LTβR) signaling. In turn, tumor HEVs boost intratumoral lymphocyte influx and foster permissive lymphocyte niches for PD1$^-$ and PD1$^+$TCF1$^+$ CD8 T cell progenitors that differentiate into GrzB$^+$PD1$^+$ CD8 T effector cells. Tumor-HEVs require continuous CD8 and NK cell-derived signals revealing that tumor HEV maintenance is actively sculpted by the adaptive immune system through a feed-forward loop.

INTRODUCTION

Immunotherapy, specifically in the form of immune checkpoint blockade (ICB), has provided unprecedented benefits, but it is effective only in a minority of cancer patients.[1,2] The limited response is in part caused by the commonly scarce T lymphocyte infiltrates (TILs),[3] while clinical responses to immunotherapy correlate with pre-existing CD8 T cell infiltration, a

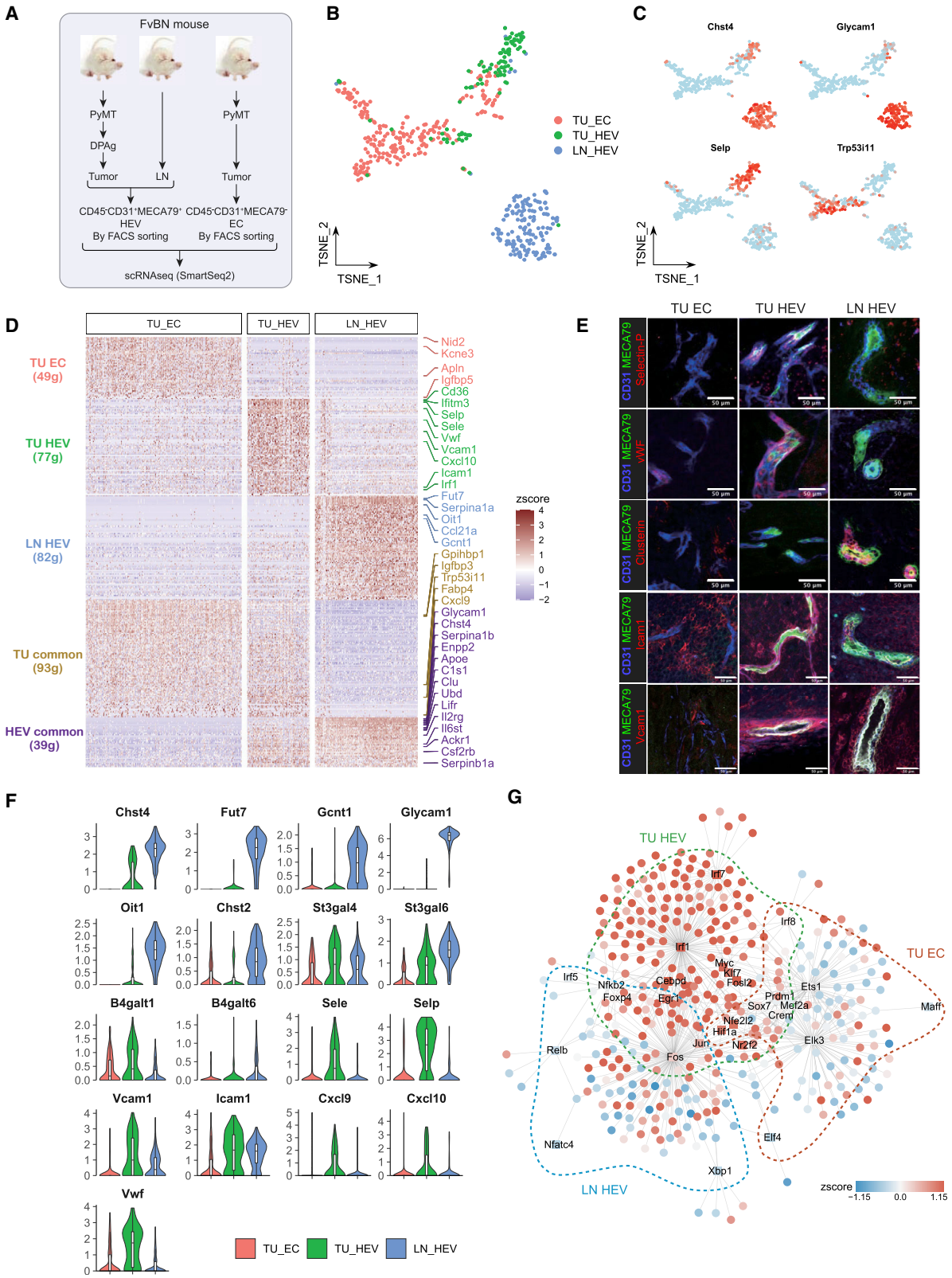

Figure 1. SmartSeq2 sequencing of TU-HEVs, LN-HEVs, and TU-ECs

(A) Study design, comparing transcriptomics of TU-HEVs, LN-HEVs, and TU-ECs.

(B and C) tSNE plot, colored by cell origins (B) or expression of representative marker genes (C).

(legend continued on next page)

T cell-instigated interferon γ (IFNγ)-induced gene signature, and neoantigen burden.[4–6] In addition, the beneficial effects of ICB and other immunotherapies may depend on the expansion and differentiation of intratumoral self-renewing $PD1^+TCF1^+TIM3^-$ progenitor CD8 T cells (pT_{EX}s) into cytotoxic $PD1^+TCF1^-TIM3^+CD8^+$ T cells (tT_{EX}s).[7–9] Lymphocytes in tumors can form aggregates coined as tertiary lymphoid structures (TA-TLSs) that have been shown to commonly associate with good prognosis, augmented patient survival, and clinical responses to chemotherapies and immunotherapies.[10,11] Although classical TLSs are well-organized structures,[12] TLSs in tumors can display a high variability of B and T lymphocyte clusters ranging from segregated to diffuse B and T lymphocyte clusters, which we refer to as tertiary lymphoid-like structures (TLLSs). It is important to note that these immune conglomerations can form only when the lymphocyte barrier properties of an angiogenic tumor vasculature, restricting the cytotoxic function of $PD1^+$ T cells and triggering apoptosis of Fas-expressing $CD8^+$ T cells, is deactivated.[13] Antiangiogenic and other vessel-normalizing therapies have been shown to reinstate T cell transmigration by enhancing lymphocyte adhesion molecules in the tumor vasculature.[14–17] This has provided a rationale for combining vascular-normalizing and immunotherapeutic approaches to sustain and improve therapeutic efficacy in cancer.[17,18] Previously, we demonstrated that antiangiogenic immunotherapies, which induced tumoral high-endothelial venules (TU-HEVs) with T cell-enriched TLLSs, exhibited an improved tumor response.[18] Indeed, TA-TLSs or tumor-associated tertiary-lymphoid-like structures (TA-TLLSs) commonly harbor HEVs uniquely poised to facilitate lymphocyte infiltration.[19,20] Under physiological conditions, HEVs reside in secondary lymphoid organs (SLOs) such as lymph nodes (LNs) to transport naive lymphocytes for priming and education. HEVs express high levels of sulphated and glycosylated ligands for lymphocyte adhesion molecules (i.e., L-Selectin/CD62L), which makes them very effective in retaining and transporting T- and B-lymphocytes.[18,21–24] The formation of TU-HEVs may provide attractive avenues to induce and sustain the efficacy of immunotherapies by overcoming the major restriction of T cell exclusion from the tumor microenvironment.

The generation and biology of TU-HEVs, however, are still poorly understood. Here, we employed single-cell RNA sequencing (scRNA-seq), *in vivo* fate mapping, and functional multiplex immune profiling to investigate the ontogeny, regulation, and function of TU-HEVs, the intimate relationship between TILs, and HEV development and function. We provide evidence that HEVs form T cell-enriched niches resembling TLLSs permissive for pT_{EX} expansion, differentiation, and activity in response to antiangiogenic immune-modulating therapies.

RESULTS

scRNA-seq identifies specific characteristics of TU-HEVs and LN-HEVs

To obtain insight into TU-HEV biology, we first assessed the phenotypic commonalities and discords between HEVs in tumors and peripheral LNs (LN-HEVs) and tumor endothelial cells (TU-ECs) by using two different approaches of single-cell transcriptional profiling. Because the triple combination of anti-vascular endothelial growth factor receptor 2 (VEGFR2, D), anti-programmed cell death ligand 1 (PD-L1, P), and lymphotoxin beta receptor (LTβR) agonist (LTβRAg) had consistently induced multiple TU-HEVs with surrounding lymphocyte infiltrates in PyMT-bearing mice, we reasoned to use this treatment strategy and model for analyzing TU-HEVs.[18] First, we isolated $CD45^-CD31^+MECA79^+$ TU-HEVs and peripheral LN-HEVs by fluorescence-activated cell sorting (FACS) using the standard MECA79 antibody that detects an HEV-specific epitope of the peripheral node addressin (PNAd),[25] the mature multivalent L-selectin ligand for lymphocyte homing. We also collected $CD45^-CD31^+MECA79^-$ TU-ECs from treatment-naive PyMT tumors by FACS and subjected all three endothelial cell (EC) populations to full-length scRNA-seq by SmartSeq2 (Figure 1A). This depicted five EC subtypes reflecting homeostatic HEVs (LN-HEVs), inflamed HEVs/postcapillary venules (PCVs; TU-HEVs), blood ECs (TU-ECs), mitotic ECs, and very few lymphatic ECs (Figures S1A and S1B). The t-distributed stochastic neighbor embedding (tSNE) plot displayed phenotypic heterogeneity with discriminative gene signatures for each EC population (Figure 1B), which we further validated with the most prominent markers by immunohistochemistry on tumor and LN sections, respectively (Figures 1C–1E).

Subsequently, differentially expressed gene (DEG) analysis (Figure 1D) confirmed that LN-HEVs displayed prominent transcriptional programs involved in glycoprotein synthesis and carbohydrate-based posttranslational modifications (Chst4, Chst2, Fut7, Gcnt1, St3gal6), as well as lymphocyte recruitment, adhesion, and diapedesis (e.g., GlyCAM1 [rodent-specific], Icam1, Vcam1, Ccl21a)[26,27] (Figures 1D–1F and S1C). As expected, a subset of TU-ECs proliferated (16%) and overexpressed endothelial tip cell markers (Kcne3, Apln, Nid2, and Trp53i110; Figure S1B), which is congruent with their overall angiogenic gene signature. TU-ECs, however, were devoid of the LN-HEV-specific gene expression profile (Figures 1D–1F and S1C). TU-HEVs, like LN-HEVs, exhibited venule markers (Ackr1, Nr2f2) and expressed Glycam1, Chst4, Fut7, Clu, Oit1, and Gcnt1, yet at lower levels (Figure 1F). Among the three EC groups, TU-HEVs exposed the highest levels of factors known to be increased during inflammation, including von Willebrand factor (Vwf), P-selectin (Selp), and E-selectin (Sele), which bind P-selectin glycoprotein ligand-1 (PSGL-1) and E-Selectin Ligand-1 (ESL-1), respectively, on activated lymphocytes and myeloid

(D) Expression of TU-EC-, TU-HEV-, and LN-HEV-specific and common genes.
(E) Immunofluorescence of selected marker genes. Scale bars, 50 μm.
(F) Violin plots of selected HEV and inflammation genes.
(G) Gene-regulatory network (GRN) predicted by SCENIC, colored by gene expression (round nodes) or regulon activity (square node) in TU-HEVs.
Population distribution and median-quantile-min/max (minimum/maximum) without outliers are shown in violin + boxplot (F). Data are from one scRNA-seq experiment. See also Figure S1.

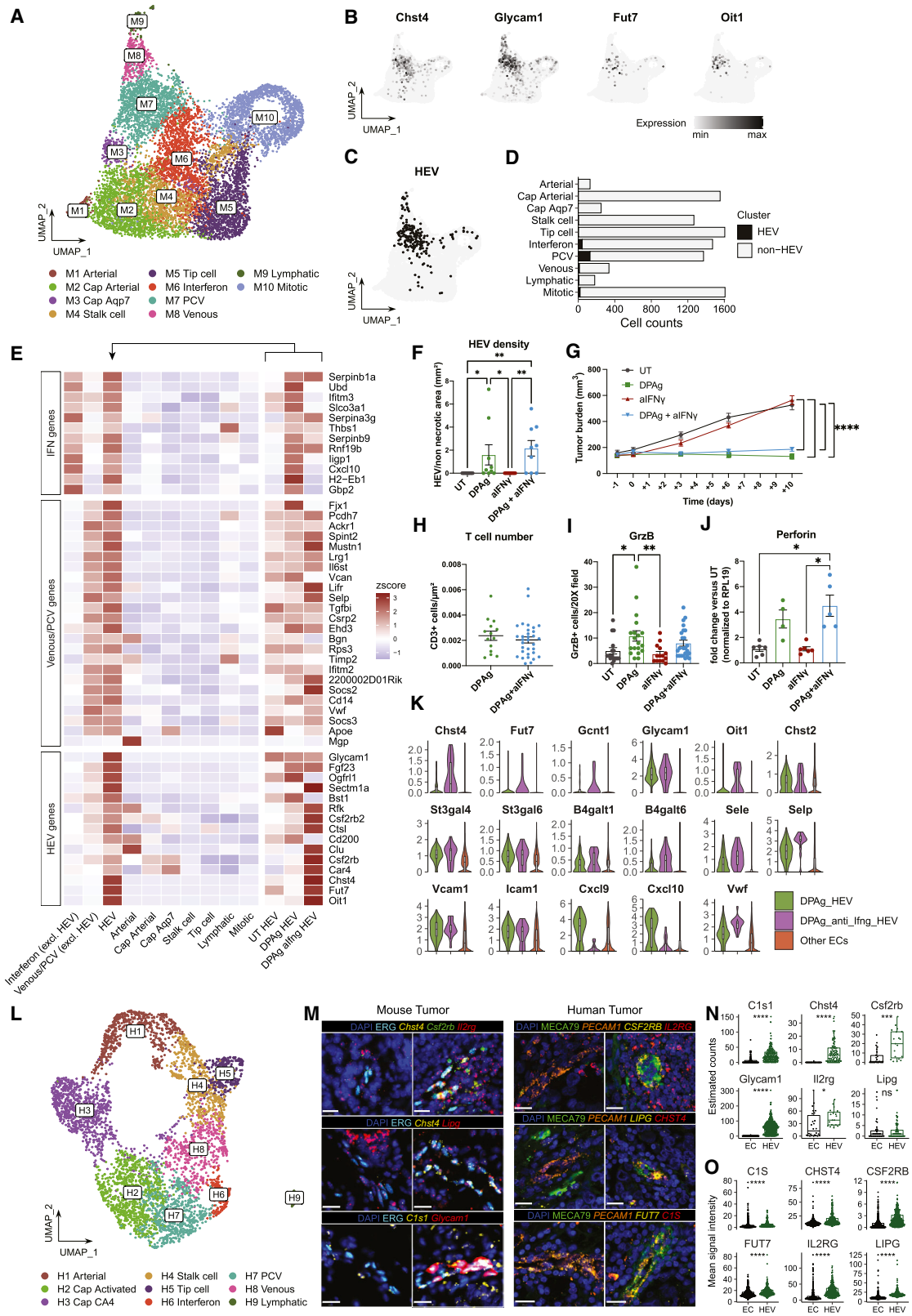

Figure 2. Characterization of the mouse and human tumor vasculature by droplet-based scRNA-seq

(A–C) UMAP plots, colored by unsupervised EC clustering in mouse PyMT and E0771 tumors (A–C), the expression of core HEV markers (B), or *in silico*-selected HEV cells (C).

(legend continued on next page)

cells. TU-HEVs also displayed elevated expression of a variety of additional genes implicated in IFN-regulated inflammation (e.g., Ifitm3, Irf1, Cxcl10) and antigen processing compared with LN-HEVs and TU-ECs (Figures 1D, 1F, 1G, and S1D). Notwithstanding, TU-HEVs and TU-ECs also shared some transcriptional similarities (e.g., Gpihbp1, Igfbp3, Cxcl9) that were absent in LN-HEVs (Figure 1D). We then inferred the main transcription factors and associated gene-regulatory networks for our different EC populations using single-cell regulatory network inference and clustering (SCENIC).[28] As expected, the regulons at play in each EC type showed commonalities but also unique differences. Besides Xbp1 and c-Fos, non-canonical nuclear factor κB (NFκB), Relb, and NFκb2 transcription factors, implicated in lymphoid organogenesis, were activated in LN-HEVs and, to a lesser extent, in TU-HEVs, while the IFN-induced transcription factor Irf1 was highly activated in TU-HEVs, confirming the gene set enrichment analysis (GSEA) results. As anticipated, transcription factors regulating angiogenesis (Maff, Ets1, and Elk3) were prevalent in TU-ECs (Figures 1G and S1E). These results display TU-HEVs as a hybrid phenotype of TU-ECs and LN-HEVs with a prominent IFNγ gene expression signature.

TU-HEVs exhibit features of inflamed postcapillary venules

Next, we conducted transcriptional profiling of the entire tumor vasculature of naive and DPAg (DC101 + anti-PD-L1 + LTβRAg)-treated PyMT, as well as E0771 breast cancers, and then assessed the presence of TU-HEVs. We also interrogated the transcriptomes of ECs from DPAg-treated PyMT tumors of mice exposed to DPAg plus anti-IFNγ treatment to assess whether IFNγ-induced inflammation affected TU-HEV formation and phenotype. TU-ECs were isolated from the different tumors and conditions by FACS ($CD45^{-}CD31^{+}$) and subjected to 10x Genomics, which yielded a total of 9,772 TU-ECs (Figures 2A and S2A). EC subtype annotation with marker genes identified from published scRNA-seq tumor endothelial datasets[29] resulted in 10 endothelial clusters (M1–10) with varying abundance: arterial ECs, two capillary subtypes (arterial and Aqp7), PCVs, venous ECs, lymphatics, tip cells, stalk cells, as well as ECs with a high IFN signature, and mitotic ECs (Figures 2A and S2B). We then identified TU-HEVs with several "HEV core markers" by detecting Chst4 co-expressed genes among highly variable genes of the entire EC population (Figure S2C). The resulting core HEV signature of the Fut7, Glycam1, Oit1, and Chst4 genes, which were also all highly expressed in LN-HEVs (Figures 1D–1F and 2B), exposed 221 TU-HEVs in the entire EC population (AUCell > 0.1; Figures 2C and S2D).[28] We found most HEVs in the cluster of PCVs, with few amid the IFN and venule EC clusters, and negligible numbers or none in the other EC subpopulations (Figure 2D). TU-HEVs depicted three distinctive expression patterns comprising a PCV/venous, IFN/inflamed, and HEV-specific gene signature (Figures 2E, S2E, and S2F). Besides the phenotypic resemblance of TU-HEVs with LN-HEVs relating to their specialized production of lymphocyte adhesion receptors, TU-HEVs expressed elevated levels of Icam1, Vcam1, Sele, and Selp and exhibited prominent activation of the major histocompatibility complex class I (MHC-I) and MHC-II antigen-processing machinery that was devoid in LN-HEVs (Figure S1D). These results confirm the SmartSeq2 data and provide further insight into the complexity of TU-HEVs.

IFNγ contributes to the disparity between TU-HEVs and LN-HEVs

The observed IFNγ response gene signature in TU-HEVs is likely caused by the proximal activated lymphocytes known to secrete IFNγ, which raises the question about the implication of IFNγ in TU-HEV genesis. Yet, DPAg immunotherapy neither altered the incidence of TU-HEV formation in PyMT-bearing mice (Figure 2F) on IFNγ depletion nor diminished the therapeutic effects of DPAg (Figure 2G). HEVs did not differ in their ability to endorse T cell influx (Figure 2H), and the T cell cytotoxic proteins granzyme B and perforin were indistinguishably upregulated in both DPAg and DPAg + anti-IFNγ tumors compared with naive tumors (Figures 2I, 2J, S2G, and S2H). Notwithstanding, blocking IFNγ increased the expression of the HEV-specific core genes (e.g., Glycam1, Oit1, Fut7, Chst4), suggesting that non-inflamed TU-HEVs become more reminiscent of homeostatic HEVs in LNs (Figures 2E and 2K). Indeed, the LN-HEV expression signature bore a significant resemblance to the one from TU-HEVs of DPAg plus anti-IFNγ-treated tumors, whereas TU-HEVs of DPAg-treated tumors shared more similarities to that of an inflamed LN-HEV transcriptome (Figures 2K and S2E).[26] In line with these results, IFNγ blockade increased expression of Glycam1, which binds L-Selectin^{+} naive T cells, and even further

(D) HEV fraction per EC subtype.
(E) Expression of TU-HEV differentially expressed genes (DEGs) and core HEV markers in tumor EC subtypes and TU-HEVs split by different treatments.
(F)Quantification of HEV density of UT, DPAg, anti-IFNγ, or DPAg plus anti-IFNγ in PyMT tumors. HEV number was determined by immunofluorescence staining with CD31 and MECA79 antibodies on frozen tissues. n tumors: 9–10.
(G) Tumor growth curves of PyMT-bearing mice treated as in (F). n tumors: 11–12.
(H) Quantification of $CD3^{+}$ T cells 50 μm around HEVs by immunofluorescence staining of DPAg or DPAg + anti-IFNγ-treated PyMT. n fields: 14–32.
(I) Quantification of $GrzB^{+}$ cells of PyMT tumors. n fields: 9–10.
(J) qPCR gene expression of perforin from total tumor lysate. n samples: 4–6.
(K) Expression of selected HEV and inflammation genes in HEVs in DPAg, DPAg + anti-IFNγ-treated tumors, and other ECs.
(L) UMAP human breast cancer EC dataset, colored by unsupervised EC clustering.
(M–O) Validation of selected conserved TU-HEV markers shared between mouse and human datasets by RNAscope. In murine PyMT (n = 1) and MC38 (n = 1) tumors, ERG and *Chst4/Glycam1* positivity identify ECs/HEVs, respectively (M, left panel), and the particle count of each RNA probe is quantified by QuPath (N). In the human breast tumor (n = 1), *PECAM1* and MECA79 positivity identify ECs/HEVs, respectively (M, right panel). Mean signal intensity of each probe in each $PECAM1^{+}$ tile was measured (O) in QuPath. Scale bars, 20 μm.
The mean ± SEM is shown (F–J). Median-quantile-min/max without outliers ± population distribution is shown in violin ± boxplot (K, N, and O). Statistics were assessed by Kruskal-Wallis test (F, I, and J), two-way ANOVA (G), Mann-Whitney test (H), and Wilcoxon test (N and O). *$p < 0.05$; **$p < 0.01$; ***$p < 0.001$; ****$p < 0.0001$. Data are pooled from at least two independent experiments (F–J) or one experiment (A–E and L–O). See also Figures S2 and S3.

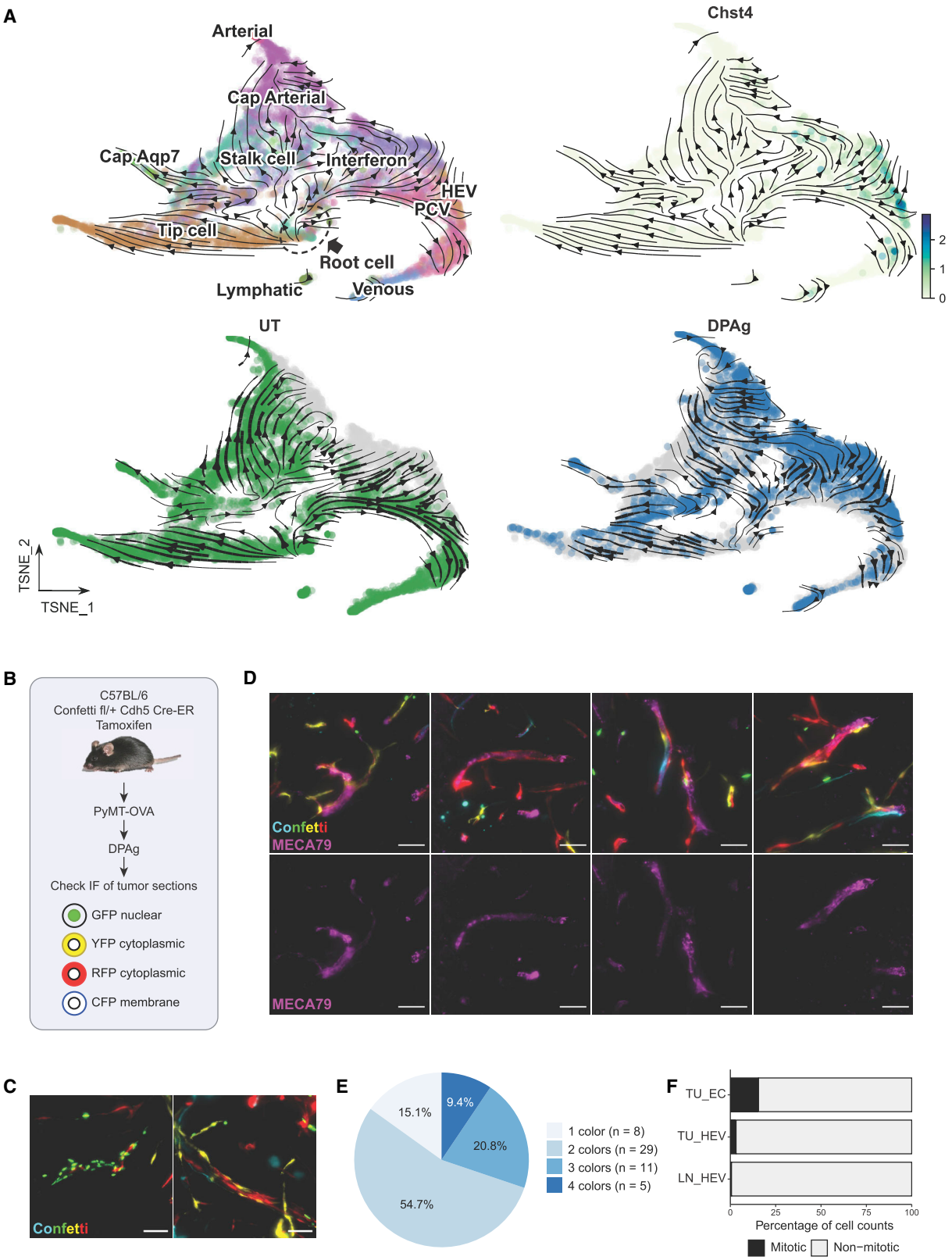

Figure 3. Ontogeny of TU-HEVs

(A) Differentiation trajectory of the tumor vasculature predicted by Velocyto/ScVelo, based on tSNE plots by Palantir. Differentiation direction is indicated by arrows in the entire datasets (top) and split by treatment groups (bottom).

(legend continued on next page)

upregulated Selp and Sele mRNA levels. This is likely due to a negative feedback loop because IFNγ has been shown to reduce Selp and Sele levels in activated ECs.[30] Overall, we did not observe significant changes in the intratumoral T cell repertoire by flow cytometry, only a slight decrease in T cell effector cells and an increase in PD1$^+$ T cells (Figures S2I and S2J).

Murine and human breast cancer ECs and HEVs share a conserved gene expression signature

Next, we set out to identify the phenotypic resemblance of the transcriptomic profile of human TU-HEVs to our murine TU-HEVs. Because we were unable to detect HEVs with our core Chst4 marker in publicly available datasets, we used scRNA-seq data from 4,621 breast cancer ECs of the BioKey breast cancer study (ClinicalTrials.gov: NCT03197389)[31] (Figure 2L). Cluster analysis revealed nine EC subtypes that were similar to those of murine tumor ECs entailing conserved markers for each mouse and human endothelial subcluster[29] (Figures 2L and S3A–S3C). Because we identified only two CHST4$^+$ ECs in the PCV cluster, which exhibited high Relb/NFκb2 activity levels like in murine HEVs (Figure S3D), we reasoned that the lack of HEVs in the human tumor samples was a combination of the overall rarity of TU-HEVs, the small tissue acquisition from needle biopsies, and the mild single-cell isolation procedures accustomed to immune cells likely unable to free HEVs from their thick vascular shafts. Because the two CHST4$^+$ ECs were insufficient to derive conclusive information about human HEVs, we set out to identify a cell cluster that shared the expression profile and Relb/Nfκb2 activities with the two CHST4$^+$ cells based on the diffusion components[32] (Figure S3E). We discovered 90 human "HEV-like" cells, which shared over 20 conserved gene signatures with mouse TU-HEVs that were significantly increased in comparison with those of human PCVs and other non-HEV EC subtypes (Figures S3F and S3G). We then selected the most conserved marker genes for both mouse and human TU-HEVs (e.g., Chst4, C1s1, Csf2rb, Il2rg) and confirmed by RNAscope that their expression in HEVs of murine tumor and human breast tumor tissues was significantly higher than in other ECs (Figures 2M–2O). These results reveal conserved transcriptional commonalities between murine and human TU-ECs that are likely also shared among TU-HEVs.

TU-HEVs are not terminally differentiated PCVs

How do HEVs then arise in the tumor vasculature? Palantir,[32] scVelo[33] (Figure 3A), and CytoTRACE analyses[34] (Figures S4A and S4B) identified a highly plastic "root cell" cluster in TU-ECs from which most trajectories started and displayed distinct differentiation routes engendering five mature states defined as tip cells, capillary Aqp7, arterial, lymphatic, and venous ECs (Figures 3A and S4B). The latter seemed to arise from a continuum of developmental stages, with PCVs depicting an intermediate state. PCVs and Chst4$^+$ HEVs, being embedded within the PCV cluster, were not recognized as terminally differentiated cell types (Figure S4B). Moreover, projections of naive and DPAg-treated TU-ECs revealed that the immune-modulating therapy significantly increased HEVs within the PCV cluster (Figure 3A). CytoTRACE confirmed the observations of "root cells" having the highest differentiation potential (DP), while the four terminal states displayed a low DP, and PCVs and TU-HEVs exhibited an intermediate score (Figure S4A). These analyses infer that TU-PCVs have the necessary plasticity to convert to TU-HEVs and do so on DPAg treatment.

TU-HEVs arise from PCVs by metaplasia

Next, we asked whether TU-HEVs emanate from PCVs via metaplasia or by clonal expansion, of which the latter may suggest the presence of a progenitor or specific EC subtype. To investigate the lineage promiscuity of TU-HEVs, we took advantage of the R26R-Confetti tracer mouse model, which enables random labeling and discrimination of individual cells with four fluorescent proteins in *cre* recombined cells[35] (Figure 3B). We generated Confetti$^{fl/wt}$ mice under the regulation of the Cdh5 (cadherin 5, also known as vascular endothelial cadherin) promoter (Confetti$^{fl/wt}$ Cdh5-CreERT2) to fluorescently label ECs on tamoxifen treatment.[35] Cdh5-CreERT2 Confetti mice were then orthotopically injected with PyMT-OVA breast cancer cells, and mice were exposed to DPAg therapy to induce TU-HEVs (Figures 3B and 3C). We then assessed the color distribution of the four fluorescent markers in 53 MECA79$^+$ TU-HEVs. Only 15% of HEVs comprised one color, while 85% of HEVs displayed two to four different colors, indicating that the majority of HEVs did not arise from clonally expanding ECs (Figures 3D and 3E). We observed areas of clonal expansion of TU-ECs (Figure 3C) reminiscent of proliferating ECs, which were, however, devoid of HEVs. These results indicate that TU-ECs transition into HEVs without the need for clonal expansion. Congruently, TU-HEVs depicted a very low proliferative rate of 3% in contrast with TU-ECs, of which 16% were mitotic (Figure 3F).

TU-EC metaplasia into TU-HEVs is dependent on immunotherapy-induced signals

To evaluate whether TU-HEVs depend on continuous therapy-induced signals, we treated PyMT and E0771 breast cancer-bearing mice with the immune-modulating DPAg therapy for 10–13 days and 8 days, respectively, then stopped the treatment and followed tumor growth for another 2 weeks (Figures 4A–4D). We determined the index and functionality of MECA79$^+$ HEVs assessed by their morphology and the number of surrounding lymphocytes and conducted a detailed immune profile of tumors at the end of treatment and 8 and 18 days after treatment cessation, as well as of naive tumors as controls (Figures 4B, 4D–4J, and S4C–S4E). The immune-modulating therapy impaired tumor growth, which was associated with substantial TU-HEV induction in both breast cancers with 30%–50% resembling enlarged

(B) Study design of Confetti tracing experiment. Recombination outcome after tamoxifen induction leads to the expression of either CFP, GFP, YFP, or RFP.
(C) Representative images of ECs after tamoxifen induction. Blood vessels with single- (left) or multiple-colored ECs (right). Scale bars, 50 μm.
(D) Representative images of MECA79$^+$ HEVs. Scale bars, 50 μm.
(E) Pie chart showing the fraction of HEV vessels found with one to four colors.
(F) Fraction of mitotic cells in TU-HEVs, LN-HEVs, and TU-ECs.
Data are pooled from at least two independent experiments (C–E) or one scRNA-seq experiment (A and F). See also Figure S4.

CellPress
OPEN ACCESS

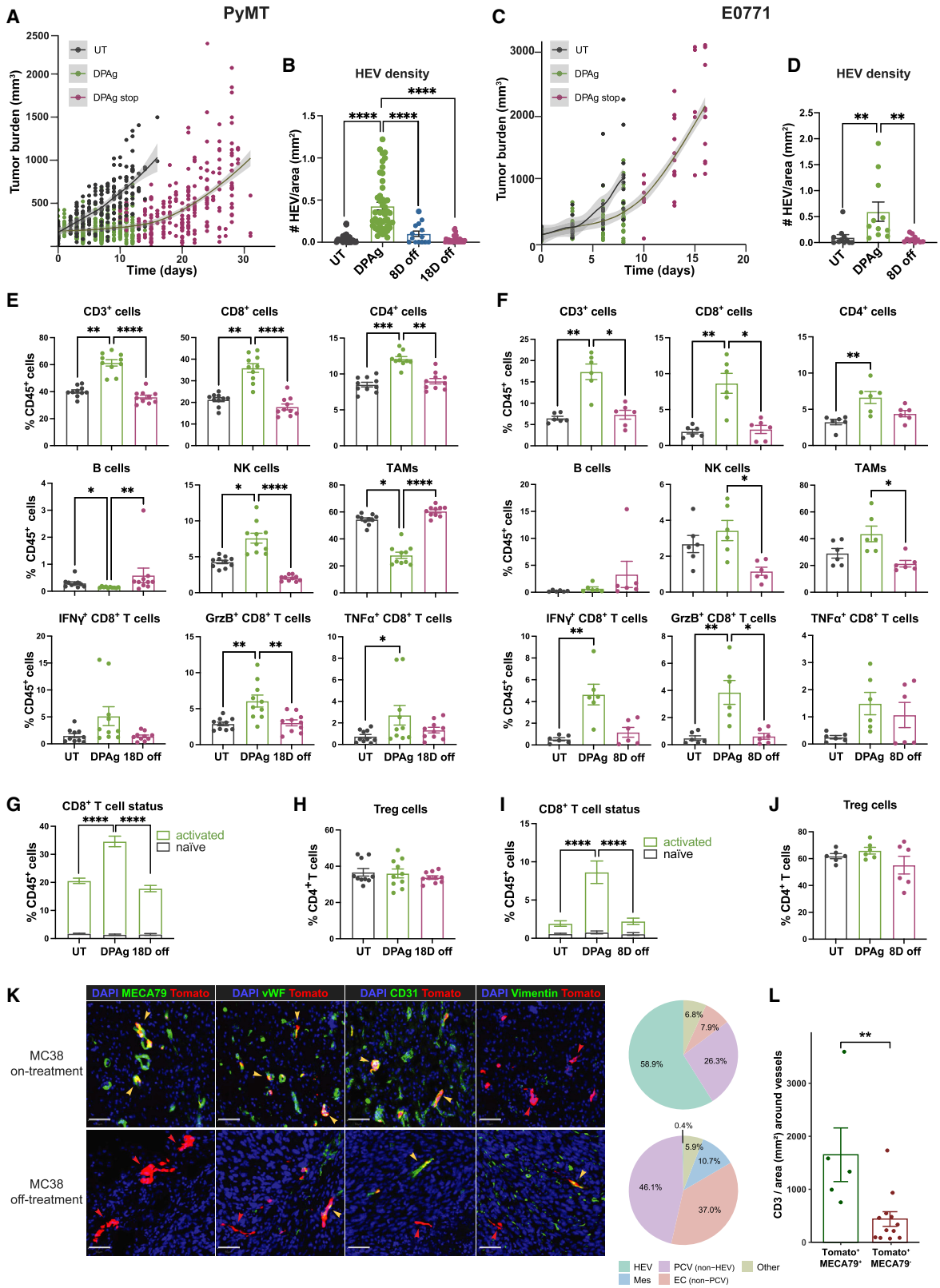

Figure 4. TU-HEVs dynamically arise on immunotherapy and require continuous signals

(A and C) Growth curve of PyMT (A) and E0771 (C) tumors during and after DPAg treatment. n tumors: untreated (UT) = 53; DPAg = 31; DPAg stop = 32 (A). n tumors: 11 for each cohort (C). 95% confidence interval (CI) of the curve is indicated by the gray line in (A).

(legend continued on next page)

and longer cuboidal-like MECA79$^+$ endothelial structures (Figures S4C and S4D) and correlated with larger surrounding lymphocyte infiltrates (Figures S4F–S4K). Focusing further into the lymphoid cell composition, TU-HEV formation was associated with an increase in intratumoral CD3, CD4, and NK cells, as well as activated cytotoxic CD8 T cells, as confirmed by IFNγ, tumor necrosis factor alpha (TNF-α), and Granzyme B (GrzB) positivity, while the percentages of B cells and CD4$^+$FoxP3$^+$ Tregs among CD4 cells were not substantially altered (Figures 4E–4J). Tumor-associated macrophages (TAMs) were reduced in PyMT tumors and slightly increased in E0771 tumors during DPAg therapy (Figures 4E, 4F, and S4E).

On treatment cessation, tumors relapsed within a week, taking up the growth rate of tumors under naive conditions (Figures 4A and 4C). Congruently, HEVs regressed in tumors within 1 week and further declined 2 weeks after therapy termination with only sparse and small MECA79$^+$ HEV structures remaining in relapsed tumors (Figures 4B, 4D, S4C, S4D, and S4F). Concomitantly, lymphocyte aggregates diminished, but the few immature MECA79$^+$ TU-HEVs that persisted after treatment stop did not lose their ability to endorse lymphocyte infiltration (Figures S4F, S4G, and S4L). Importantly, the TU-HEV decline was associated with an overall decrease in intratumoral CD4, NK cells, and activated CD8 T cells that reverted to levels similar to those observed in naive tumors (Figures 4E–4G, 4I, and S4E).

TU-HEVs dynamically arise on immunotherapy and require continuous signals

We then inquired about the fate of TU-HEVs on therapy cessation by genetically tracking TU-HEVs. We generated Chst4-CreER C57BL/6 mice, which enable Cre-mediated gene deletion in Chst4$^+$ HEVs, and bred them to Rosa26$^{LSL\text{-}tdTomato(tdT)}$ mice (Chst4-tdT) in which Cre induces tdT expression in HEVs on tamoxifen administration and remains expressed independently of cell fate. We treated Chst4-tdT mice bearing PyMT-OVA or MC38 tumors with tamoxifen and either DCAg (anti-cytotoxic T-lymphocyte-associated protein 4 [CTLA-4] instead of anti-PD-L1) or anti-CTLA-4 + LTßRAg (CAg) for 9 or 11 days, respectively, to ensure the efficient formation of tdT-labeled HEVs (on treatment) (Figures 4K, S4M, and S4N). The reasoning for including anti-CTLA-4 antibody is based on our later observations that Treg inhibition with anti-CTLA-4 furthered LTßRAg-induced HEV formation, and that Treg depletion can induce spontaneous TU-HEVs.[36] On treatment cessation, tumors of the on-treatment group were immediately analyzed, whereas tumors of the off-treatment groups were evaluated 11 days after therapy termination when HEVs had diminished (Figures 4K, S4M, and S4N). Immunofluorescence staining of on-treatment tumors confirmed the appearance of multiple tdT-labeled MECA79$^+$ TU-HEVs (Figures 4K and S4M), whereas tumors at the off-treatment time point contained a sparse population of tdT$^+$ MECA79$^+$ cells (Figures 4K and S4N). Several tdT$^+$/MECA79^{neg} cells were identified at the tumor rim, where HEVs are commonly found, and some were randomly distributed within the tumor core. Because MC38 tumors contained substantially more tdT$^+$ cells than PyMT-OVA tumors, we investigated the cell fate of the tdT-labeled cells in MC38 tumors by immunofluorescence staining (Figure 4K). In the on-treatment setting, most tdT$^+$ cells displayed HEVs, and only a minor subset of CD31$^-$tdT$^+$ cells (6.8%) that had lost their EC phenotype were identified in the tumor center. In the off-treatment setting, only 0.4% of tdT$^+$ cells remained as HEVs, whereas most tdT$^+$ cells expressed markers of PCVs (46.1%) or other EC types (37.0%), confirming that on treatment cessation, HEVs transition back into a normal EC/PCV state. Furthermore, approximately 15% of tdT$^+$ cells lost their endothelial phenotype, with about 10% undergoing an endothelial to mesenchymal transition (EndMT) as they expressed the mesenchymal marker vimentin (Figure 4K). Finally, we tested whether the conversion of tdT$^+$ HEVs to tdT$^+$ ECs affected the surrounding lymphocyte landscape. Although tdT$^+$ HEVs elicited substantial CD3$^+$ T lymphocyte aggregates, their transition into tdT$^+$ ECs diminished surrounding lymphocytes (Figures 4L and S4O). Thus, the immune-modulating therapy not only rapidly induced HEV formation and subsequent lymphocyte infiltration but also was necessary to maintain HEVs and their lymphocyte aggregates because they precipitously diminished on treatment termination, concordant with tumor relapse.

CD8 T cells and NK cells induce therapeutic TU-HEV formation via the LT/LTßR axis

Based on these results, we speculated that a feed-forward loop is the underpinning mechanism of HEV-induced lymphocyte aggregation. Because various immune cells are involved in LN development and LN-HEV maintenance, and lymphocytes appear to regulate spontaneous HEV formation in tumors, together with the strong correlation of lymphoid cells surrounding therapeutically induced TU-HEVs, we reasoned that recruited lymphoid cells might also provide the necessary HEV-inducing signals during immunotherapy.[19,36–40] In support, DPAg treatment of PyMT tumor-bearing Rag knockout (KO) mice did not induce TU-HEVs and was rather ineffective,

(B and D) Quantification of TU-HEV density in PyMT (B) or E0771 (D) tumors by immunofluorescence tissue staining. n tumors: UT = 10; DPAg = 10; DPAg 8 days [8D] off = 4; 18 days [18D] off = 10 (B). n tumors: 11 for each cohort (D).

(E–J) Immune cell characterization of PyMT (n = 10 for each cohort) (E, G, and H) or E0771 (n = 6 for each cohort) (F, I, and J) tumors on DPAg treatment or after treatment cessation (8D off or 18D off) by flow cytometry. CD62L staining was used to discriminate naive (CD62L$^+$) CD8 T cells from the activated (CD62L$^-$) CD8 T cells (G and I).

(K and L) Immunofluorescence staining and quantification of MC38 tumor sections from Chst4-tdT reporter mice on anti-CTLA-4 + LTßRAg (CAg) treatment (treatment ON) or after treatment cessation (treatment OFF). (K) Representative images of MECA79/vWF/CD31/Vimentin staining, and quantification of percentage of each subtype (HEV/PCV/EC/Mesenchymal/Other) among total tdTomato$^+$ structures during treatment ON or OFF (n = 2). Yellow and red arrowheads depict double- and single-labeled cells, respectively. Scale bars, 50 μm. (L) Quantification of CD3 density within 50 μm of MECA79$^+$ or MECA79$^-$tdTomato$^+$ vessels.

95% CI of the curve is indicated by the gray line in (A). The mean ± SEM is shown (B, D, E–J, and L). Statistics were assessed by Kruskal-Wallis test (B, D, and E–J) or Wilcoxon test (L). Only statistical differences UT versus DPAg, DPAg versus 18D off, and DPAg versus 8D off are shown (E–J). *$p < 0.05$; **$p < 0.01$; ***$p < 0.001$; ****$p < 0.0001$. Data were pooled from at least two independent experiments (A–J) or one experiment (K and L). See also Figure S4.

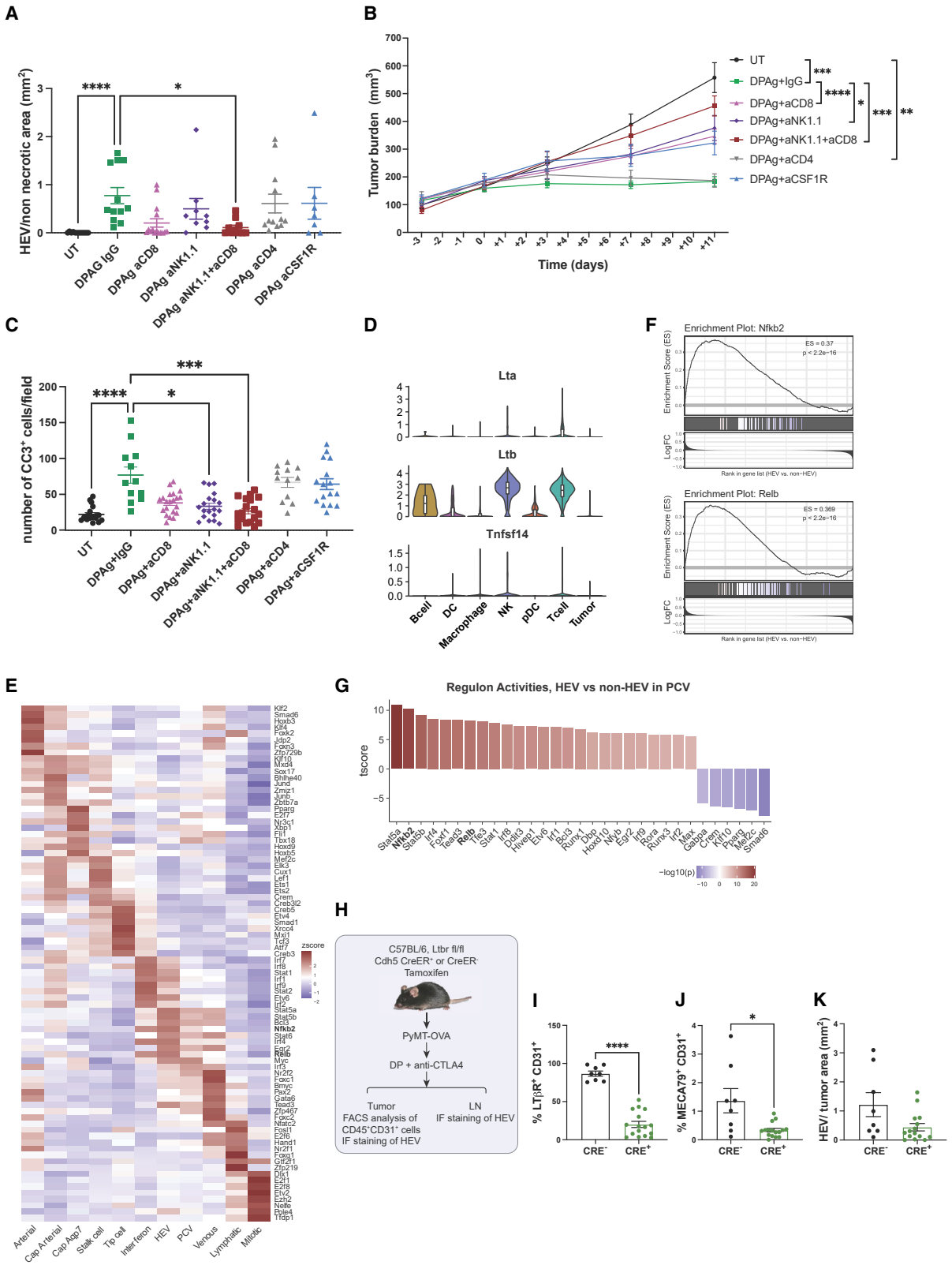

Figure 5. CD8 T cells and NK cells induce immunotherapy-dependent HEV formation via the LT/LTβR axis

(A–C) TU-HEV density (A, n = 7–15), tumor growth curve (B, n = 6–15), and apoptotic index (C, n = 12–21) of PyMT-bearing mice treated with DPAg and depleted of CD8, CD4, NK cells, or macrophages by administration of anti-CD8, anti-CD4, anti-NK1.1, and anti-CSF1R, respectively.

(legend continued on next page)

supporting the requirement of adaptive immune cells (Figures S5A and S5B). Flow cytometry analysis of the PyMT and E0771-infiltrating immune cell repertoire revealed a negligible percentage of $CD25^+CD127^+ROR\gamma t^+$ ILC3 cells, the adult counterpart of lymphoid tissue inducer (LTi) cells known to instigate LN development (Figures S5C–S5G).[40] The plasmacytoid dendritic cells (pDCs), conventional type 1 dendritic cells (cDC1s), and conventional type 2 dendritic cells (cDC2s) were also rather low and, except for cDC2 in E0771 tumors, did not substantially increase on DPAg therapy (Figures S5H–S5J). We then assessed TU-HEV induction in wild-type (WT) and CD4 T cell, CD8 T cell, NK cell, or macrophage-depleted PyMT tumors in response to DPAg therapy. Depleting CD4 T cells or $CSF1R^+$ macrophages did not alter HEV density and treatment effects (Figures 5A and 5B). However, abrogating CD8 T cells or NK cells reduced HEVs, and their combined depletion ebbed HEVs to levels of control IgG-treated tumors and rendered tumors nearly ineffective to the immunotherapy with a low apoptotic tumor index comparable with that of control tumors (Figures 5A and 5C). Thus, TU-HEV formation required CD8 T cells and NK cells, which directly correlated with the beneficial effects of antiangiogenic immunotherapy. Do then these cells provide signals that are conducive to HEV conversion? NicheNet analysis[41] of the scRNA-seq data revealed IFNγ and lymphotoxin-α and -β (LTα and LTβ) as the top-ranked ligands being highly expressed by NK and T cells (Figures 5D and S5K). Using SCENIC, we further found that the LT/LTβR-induced key transcription factors of the noncanonical NFκB pathway, Nfκb2, and Relb exhibited increased activity enhancing expression of their target genes in HEV cells, but not in non-HEV EC cells (Figures 5E and 5F), congruent with the upregulation of other constituents of the LTβR-noncanonical NFκB axis (Figure 5G). We then treated PyMT-OVA or MC38 tumor-bearing $LT\beta R^{ECKO}$ mice with a combination of DC101, anti-PD-L1, and anti-CTLA-4 (DPC) antibodies (Figures 5H–5K, S5L, and S5M), which induced HEVs in WT mice, but not in $LT\beta R^{ECKO}$ tumor-bearing mice (Figures 5J and 5K). Consistent with former reports, endothelial LTβR deficiency also decreased HEV density in LNs within 2 weeks (Figure S5N).[26] Because the recombination efficiency among tamoxifen-treated Cdh5-CreER $LT\beta R^{fl/fl}$ mice was quite variable (50%–90%) (Figure 5I), we investigated whether the few TU-HEVs in some of the PyMT-$LT\beta R^{ECKO}$ mice arose from the remaining LTβR WT or deficient ECs. We bred the Cdh5-CreER-$LT\beta R^{fl/fl}$ to the $Rosa26^{LSL\text{-}tdTomato(tdT)}$ mice, which on tamoxifen exposure fluorescently labeled LTβR-KO, but not WT, ECs. These experiments confirmed that antiangiogenic immunotherapy induced $MECA79^+$ TU-HEVs in LTβR WT ECs with few HEVs also arising from LTβR KO ECs (Figure S5O). In summary, CD8 T cells and NK cells provide LTα1β2 lymphotoxins to activate the LTβR/noncanonical NFκB axis in TU-ECs that subsequently induces TU-HEVs.

These results further rationalize the use of the LTβRAg in inducing HEVs, but to which extent does antiangiogenic therapy aid the therapy? We investigated the contribution of the single DC101 and LTβRAg regimens and compared them with the combined therapy in MC38- and E0771-bearing mice. Tumor burden was moderately reduced by DC101 and slightly more lessened by LTβRAg, but the combined treatment significantly impaired tumor growth (Figures S6A and S6B). As expected, anti-VEGFR2 therapy itself had vessel-normalizing properties but was not sufficient to induce HEVs (Figures S6C–S6E). However, it substantially enhanced the HEV-inducing properties of the LTβRAg (Figures S6A–S6H), which by itself also enhanced vessel normalization and perfusion (Figures S6D and S6E). Thus, DC101 plus LTβRAg exhibited the highest degree of vessel perfusion, vessel normalization, lymphocyte influx, and subsequent tumor growth reduction compared with single treatments (Figures S6B–S6G).

TU-HEVs generate lymphocyte niches permissive for $TCF1^+$ CD8 progenitor cells

Do TU-HEVs then act as mere lymphocyte portals, or can they also form lymphocyte niches that are permissive for T cell expansion? Most CD8 T cells expressed PD1 in PyMT and E0771 tumors and increased to about 80%–90% during DPAg treatment (Figures 6A and S7A) concomitant with elevated levels of IFNγ and TNF-α or GrzB or IL-2, exhibiting a "polyfunctional" phenotype that has been associated with better tumor control (Figures 6B, S7B, and S7C).[42,43] We then determined the levels of pT_{EX}s and tested whether pT_{EX}s increase during antiangiogenic immunotherapy, accumulate in HEV^+ lymphocyte niches, and differentiate into tT_{EX}s.[43] $PD1^+$ CD8 cells entailed 10% of pT_{EX}s and 16% of tT_{EX}s, of which the latter nearly doubled during DPAg treatment (Figures 6C, 6D, and S7D). $TCF1^-TIM3^-$ CD8 T cells comprised most $PD1^+$ CD8 T cells (Figures 6D and S7D). Only a few $TCF1^-TIM3^-$ CD8 T cells and pT_{EX}s expressed GrzB, but pT_{EX}s were more proliferative than tT_{EX}s and $TCF1^-TIM3^-$ CD8 T cells and produced IFNγ and perforin (Figures 6E–6G). $TCF1^+PD1^-$ CD8 T cells constituted about 15%–30% of CD8 T cells (Figure 6H), but they did not increase on treatment, while about double as many $TCF1^+PD1^-$ CD8 T cells were $GrzB^+$ on DPAg treatment (Figures 6H–6J and S7E).

Congruent with the flow cytometry analysis, we identified three major CD8 clusters from the RNA-seq data; i.e., naive/early activated CD8 cells being $PD1^-$, $CD44^-$ $Tcf7^{+/lo}$ (encoding TCF1), $GrzB^+$, $CCR7^+$, pT_{EX}, and tT_{EX}. The proximity of pT_{EX}s and tT_{EX}s on the uniform manifold approximation and projection (UMAP)

(D) Violin plot of Lta (LTα), Ltb (LTβ), and Tnfsf14 (LIGHT) expression in each immune cell cluster from the E0771 and PyMT dataset.
(E) TF activities in each EC subtype predicted by SCENIC.
(F) GSEA plots of Nfkb2 and Relb-regulated target genes in HEVs versus non-HEV ECs. Kolmogorov-Smirnov Tests.
(G) Waterfall plot, comparing regulon activities of TU-HEVs and non-HEV ECs in PCVs predicted by SCENIC.
(H) Experimental design of HEV evaluation in PyMT $LT\beta R^{ECKO}$ mice.
(I–K) Quantification of $LT\beta R^+CD31^+$ (I) and $MECA79^+CD31^+$ cells (J) by flow cytometry, and quantification of $MECA79^+CD31^+$ tumor vessels by immunofluorescence staining (K) of PyMT-OVA-bearing Cdh5-Cre^{ER} × $LT\beta R^{fl/fl}$ (CRE^+) or control (CRE^-) mice treated with DC101 + anti-PD-L1 + anti-CTLA-4 (DPC). n tumors: CRE^- = 8; CRE^+ = 16 (I and J). n tumors: CRE^- = 8; CRE^+ = 15 (K). The mean ± SEM is shown (A–C and I–K). Population distribution and median-quantile-min/max without outliers are shown in violin + boxplot (D). Statistics were assessed by Kruskal-Wallis test (A and C), two-way ANOVA (B), and Mann-Whitney test (I–K). Only statistical differences UT versus DPAg IgG and DPAg IgG versus DPAg immune cell-depleted tumors are shown in (A)–(C). *$p < 0.05$; **$p < 0.01$; ***$p < 0.001$; ****$p < 0.0001$. Data are pooled from two independent experiments (A–C and I–K) or one scRNA-seq experiment (D–G). See also Figures S5 and S6.

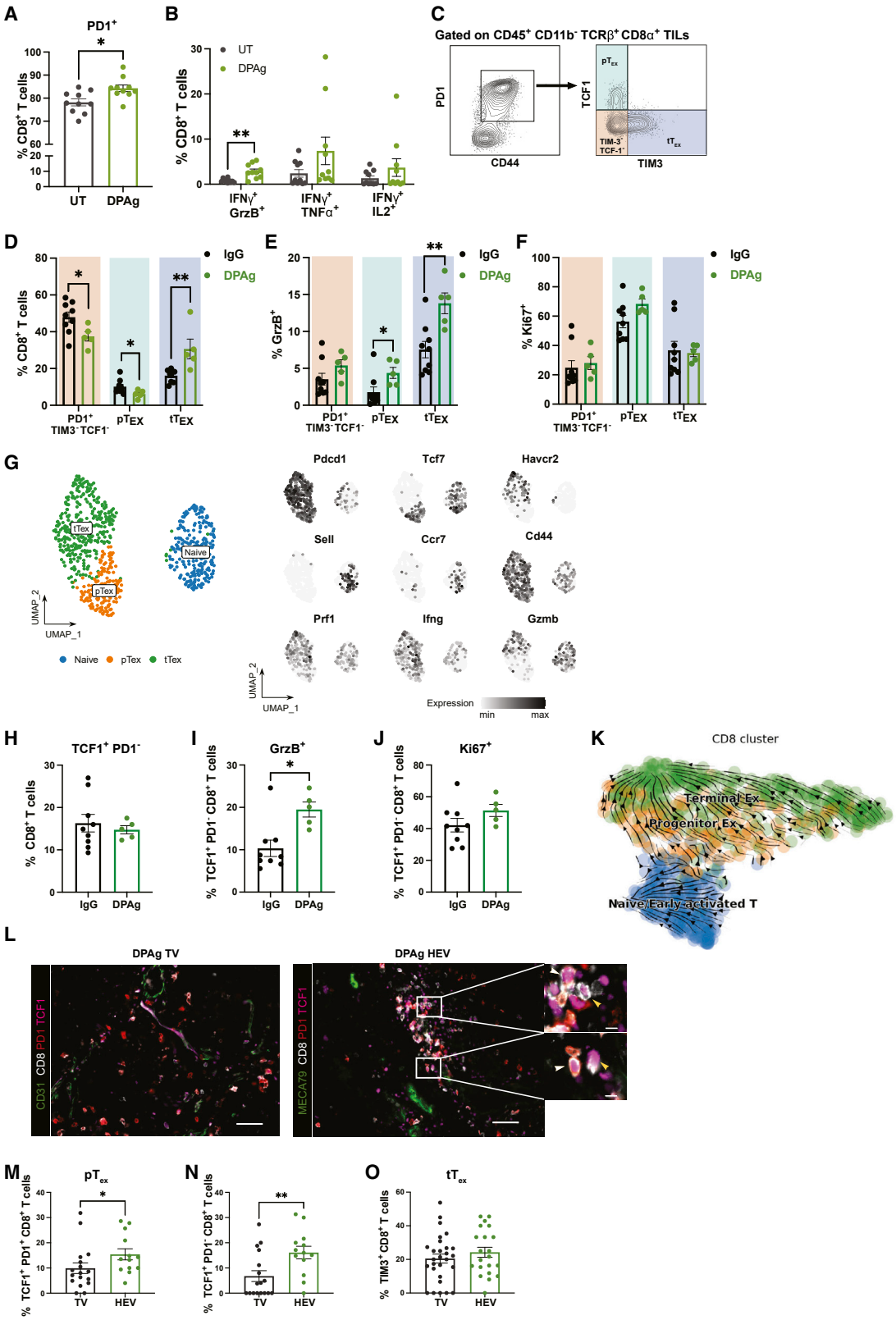

Figure 6. TU-HEVs generate lymphocyte niches permissive for PD1^{neg} and PD1^{+} CD8 progenitor cells

(A and B) Flow cytometry quantification of PD1^{+} CD8 T cells (A) and CD8 T cells co-expressing IFNγ-GrzB, IFNγ-TNF-α, or IFNγ-IL2 (B) in UT (n = 10) and DPAg-treated (n = 10) PyMT tumors.

(legend continued on next page)

confirmed the transcriptional similarity between these populations, consistent with the previously proposed lineage relationship between pT_{EX}s and tT_{EX}s (Figure 6J).[9,43] Trajectory of the three distinct CD8 populations displayed that most pT_{EX}s transitioned into tT_{EX}s, whereas only a very small subset of naive/early activated T cells became effector CD8 T cells (Figure 6K). Because these analyses gave only an inkling about the overall CD8 T cell composition and activity within the tumor, we assessed whether these changes occurred in the TU-HEV-associated lymphocyte aggregates. Indeed, pT_{EX}s and $PD1^{-}TCF1^{+}$ CD8 T cells preferentially surrounded TU-HEVs (Figures 6L–6N, S7F, and S7G). Consistent with a previous report, tT_{EX}s were more broadly distributed within the tumors and therefore did not display significantly different numbers between tumor vessels and HEVs of treated tumors[9] (Figures 6O and S7H).

We then employed the MILAN multiplex immunohistochemistry platform to analyze the numbers, proliferative index, and cytolytic index of the following specific CD8 T cell subpopulations: $TCF1^{+}PD1^{-}TIM3^{-}$ CD8 T cells, $TCF1^{+}PD1^{+}TIM3^{-}$ CD8 T cells (pT_{EX}s), $TCF1^{-}PD1^{+}TIM3^{+}$ CD8 T cells (tT_{EX}s), and not-otherwise-specified CD8 T (T_{NOS}) cells in relation to the presence or absence of TU-HEVs, as well as the distance to HEVs, by maintaining spatial resolution (Data S1).[44] Digital reconstruction of MC38 tumors of LTβRAg and anti-CTLA-4-treated mice revealed multiple $MECA79^{+}$ HEV clusters at the tumor rim and in peritumoral areas (Figures S7I–S7L). Two expert pathologists (F.M.B. and G.F.) manually and independently annotated the tumor bulk, tumor edge, and peritumor areas. We identified a total of 40,930 CD8 T cells in the four MC38 tumors, of which 1.83% displayed pT_{EX}s, 10.84% $TCF1^{+}PD1^{-}$ T cells, and 26.23% tT_{EX} cells, while 61.09% comprised CD8 T_{NOS} cells. pT_{EX}s and $TCF1^{+}PD1^{-}$ CD8 cells were more abundant in HEV-high areas at the tumor edge and in the peritumoral area (where HEVs are normally found), whereas tT_{EX} cells prevailed more in HEV-low areas and the tumor bulk (Figures 7A and S7L). The remaining T_{NOS} cells did not show any prevalent location (Figure 7A). Interestingly, pT_{EX}s proliferated more in HEV-high areas than in HEV-low locations, but $TCF1^{+}PD1^{-}$ CD8 T cells and tT_{EX}s were, in general, less proliferative (Figure 7B). In contrast, most tT_{EX}s expressed the cytolytic enzyme GrzB, particularly in the tumor bulk and in HEV-low areas, but to a lower extent in HEV-high tumors (Figure 7B). Together, these results infer that therapeutically induced HEVs support the formation of lymphocyte niches in which pT_{EX}s can self-renew and produce $GrzB^{+}$ tT_{EX}s, which produce more GrzB with increasing distance from HEVs.

Next, we set out to investigate the commonalities of HEV^{+} niches in human cancer with the MILAN platform by focusing on the same CD8 T cell subpopulations in HEV^{+} human tumor sections from six treatment-naive luminal, $Her2^{+}$, and triple-negative breast cancer patients. Like in murine tumors, HEV-high areas were preferentially located at the tumor rim or in the peritumoral area entailing a conglomeration of CD8 T cells, including prevalent populations of pT_{EX}s and $PD1^{-}TCF1^{+}$ cells (Figures 7C and 7D). Whereas pT_{EX}s and $PD1^{-}TCF1^{+}$ T cells were in close proximity to HEVs, tT_{EX}s were more common on the outskirts of HEV niches and in non-vascular and tumor bulk areas (Figures 7A, 7C, and 7E). Like in murine TU-HEV niches, pT_{EX} proliferation climaxed in HEV-high locations, whereas $PD1^{-}TCF1^{+}$ and T_{NOS} cells were poorly proliferative independent of their locations. We, however, also observed differences as human tT_{EX}s proliferated more than their murine counterparts and expressed more GrzB and perforin in peritumoral and non-vascular areas, but not in the tumor bulk (Figures 7B and S7M). This may not be unexpected because the majority of tT_{EX}s in human tumors have likely not undergone full maturation and differentiation under treatment-naive conditions. Taken together, we have identified HEV niches at the rim of murine and human tumors that, besides $PD1^{-}TCF1^{+}$ T cells, harbor proliferative pT_{EX}s that give rise to cytotoxic effector CD8 T cells (Figure 7F).

Human HEV signature correlates with response to ICB therapy

Because HEVs generate immune cell-promoting niches, it is conceivable that the presence of HEVs in malignant lesions may increase the probability of a response to ICB therapy in patients. We first defined a compelling human HEV signature based on conserved HEV genes between mouse and human tumors and human LNs (Figures 2M–2O, S3F, and S3G). Next, we assessed whether the selected human TU-HEV gene signature (CHST4, FUT7, LIPG, ENPP2, LIFR, CH25H, C4BPA, ENPP6) is enriched in melanoma and non-small cell lung cancer (NSCLC) patients responding to ICB therapy using publicly available transcriptomic datasets.

In the CA209-038 study, 68 melanoma patients were treated with nivolumab.[45] Whereas biopsies of non-responders (PD) had a low HEV gene enrichment signature (gene set variation analysis [GSVA] score), which did not increase during treatment, biopsies from patients with stable disease exhibited a significant HEV increase during treatment (Figure 7G). Furthermore, partial responder/complete responder (PR/CR) responding patients

(C) Gating strategy for intratumoral $PD1^{+}TCF1^{-}TIM3^{-}$ cells, $PD1^{+}TIM3^{-}TCF1^{+}$ pT_{EX}s, and $PD1^{+}TCF1^{-}TIM3^{+}$ tT_{EX}s.
(D and H) Flow cytometry quantification of $PD1^{+}TCF1^{-}TIM3^{-}$ cells, pT_{EX}s, tT_{EX}s (D), and $TCF1^{+}PD1^{-}$ cells (H) in IgG (n = 9) and DPAg (n = 5) PyMT tumors.
(E, F, I, and J) Flow cytometry quantification of $GrzB^{+}$ (E and I) and $Ki67^{+}$ (F and J) $PD1^{+}TCF1^{-}TIM3^{-}$ cells, pT_{EX}s, and tT_{EX}s (E and F) or $TCF1^{+}PD1^{-}$CD8 T cells (I and J) from IgG-treated (n = 9) and DPAg-treated (n = 5) PyMT tumors.
(G) UMAP of CD8 T cell subsets in the PyMT dataset (left) and selected genes (right).
(K) Differentiation trajectory inference by Velocyto/ScVelo.
(L) Representative images of PyMT tumors from DPAg-treated mice. The scale bars indicate 50 μm. White arrowheads depict pT_{EX} cells; yellow arrowheads depict $TCF1^{+}PD1^{-}$ cells. Scale bars in the selections indicate 10 μm.
(M–O) Percentage of pT_{EX}s (tumor vessel [TV], n = 17; HEV, n = 13) (M), $TCF1^{+}PD1^{-}$CD8 T cells (TV, n = 17; HEV, n = 13) (N), and tT_{EX}s (TV, n = 27; HEV, n = 21) (O) among all CD8 T cells within 50 μm of HEVs or TVs in tumor sections of DPAg-treated PyMT-bearing mice.
The mean ± SEM is shown (A, B, D–F, H–J, and M–O). Mann-Whitney test (A, B, D–F, H–J, and M–O). *$p < 0.05$; **$p < 0.01$. Data are pooled from at least two independent experiments (A, B, D–F, H–J, and M–O) or one experiment (G and K). (G and K) Derived from the UT and DPAg-treated PyMT tumors. See also Figure S7.

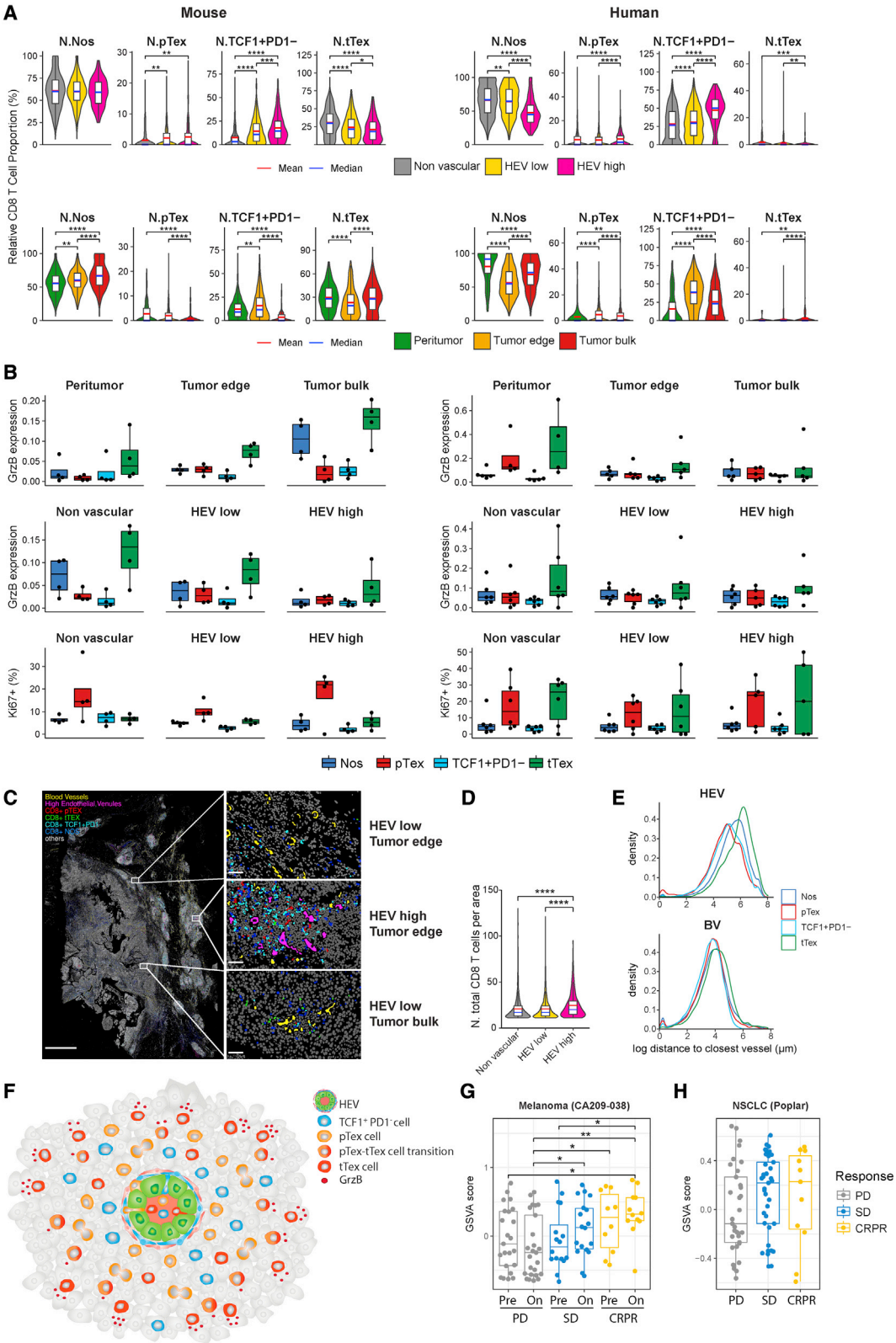

Figure 7. Immune and vascular landscape by MILAN

(A) The relative proportion of different CD8 T cells within mouse MC38 tumors (left) and human breast cancer (right).

(B) GrzB expression and Ki67^{+} percentage of the CD8 T cell subsets within mouse MC38 tumors (left) and human breast cancer (right).

(legend continued on next page)

displayed the highest HEV score, which, importantly, was already elevated in pretreated biopsies (Figure 7G). Similar correlations with an increased HEV gene enrichment signature in responding patients were observed in the POPLAR datasets from 81 NSCLC patients treated with atezolizumab (Figure 7H)[46,47] and in the PCD4989g datasets of 54 atezolizumab-treated NSCLC patients (Figure S7N).[47,48] These results support the proposition that the presence of TU-HEVs is associated with a better response to ICB in melanoma and NSCLC patients and further corroborate HEVs as decisive benefactors of immune responses in cancer.

DISCUSSION

The lack of sufficient infiltration of tumor-reactive lymphocytes is a major obstacle in immunotherapy. Here, we show that therapeutic induction of HEVs (TU-HEV) via angiogenic ICB or ICB combination therapies in cancer augments lymphocyte entry and contributes to tumor growth inhibition by generating TLLSs, along with $TCF1^+CD8^+$ T cell niches, that produce GrzB-secreting tT_{EX}s. Although direct evidence demonstrating a corroborative role of TU-HEVs and TLLS formation in boosting immunotherapies remains to be seen, various studies have revealed a strong association between these structures in benefiting cancer patients. Not only have they been commonly identified within lymphocyte-rich areas in human cancers and correlated with prolonged metastasis-free, disease-free, and overall survival rates of metastatic melanoma, breast, and gastric cancer patients,[19] but our retrospective analysis of an HEV signature in tumor samples of NSCLC and melanoma patients undergoing ICB, together with the strong correlation of HEVs in melanoma tissues of ICB responders,[49] underscores the significance of TU-HEVs in increasing the probability of tumor response to ICB.

We observed that the lymphocyte aggregates surrounding TU-HEVs were all predominantly composed of diffuse T cell aggregates and fewer B cells with multiple $MHC\text{-}II^+$ myeloid cells in the different tumor types undergoing antiangiogenic immune-modulating therapies. These resembled the dense aggregates of $MHC\text{-}II^+$ APCs and CD8 T cells that had recently been discovered in human renal cell carcinomas (RCCs) and were distinct from the typical B cell-germinal centers identified in TLSs of RCCs.[7] Moreover, this study paralleled our results of increased numbers of pT_{EX}s, giving rise to terminally differentiated tT_{EX}s in the CD8 T cell-enriched areas.[7,43] Recently, both pT_{EX}s and $PD1^-TCF1^+$ CD8 T cells have been described as self-renewing precursor populations that expanded and differentiated into $TCF1^{neg}$ CD8 effector-like cells on treatment with ICB producing a continuous pool of newly differentiated effector $CD8^+$ T cells.[8,9] We observed that pT_{EX}s were more abundant and proliferative in HEV-high than HEV-low areas of murine and human tumors. Notably and in agreement with ICB-promoting $TCF1^+$ T cell expansion and differentiation, these phenotypes were more prevalent in ICB-treated murine tumors than in treatment-naive human breast cancers. Because tT_{EX}s displayed augmented GrzB levels with increasing distance from HEVs in ICB-treated tumors, it is tempting to speculate that tT_{EX}s surrounding HEVs are at an early stage of differentiation, just being produced by pT_{EX}s, and exhibit more cytotoxic T lymphocyte (CTL) activity on maturation while they are migrating into the tumor bulk.

TU-HEV induction depended on an immunostimulating environment in which continuous signals emanating from activated lymphocytes and NK cells were required and are consistent with the observed paracrine signaling loop between ECs and activated lymphocytes, not only in treated but also in naive tumors.[39] Anti-VEGFR2 therapy itself was not sufficient to induce HEVs, but it substantially enhanced the HEV-inducing properties of the LTβRAg therapy. A strong causal link between vessel normalization and HEV/TA-TLLS formation was also demonstrated in pancreatic neuroendocrine tumor (PNET)-bearing Rip1Tag5 mice, which were treated with a tumor vessel-binding peptide of LIGHT (LIGHT-VTP), another ligand for LTβR. Moderate LIGHT-VTP administration induced mature TA-TLSs in direct correlation to the extent of vessel normalization.[37,50] Thus, vessel normalization, albeit insufficient, can instigate steps in supporting HEV and TA-TLLS formation. In addition, it is conceivable that any therapy that enhances lymphocyte entry may be an initiating and supporting step to raise lymphocytes to the threshold that yields endothelial conversion into HEVs. HEVs then amplify this feed-forward loop by further enhancing lymphocyte infiltration. In support, combined inhibition of leukocyte phosphatidylinositol 3-kinase δ (PI3Kδ) or interleukin-15 (IL-15)-expressing oncolytic adenoviruses also promoted TU-HEV and TLLS formation with lymphocyte influx in mouse tumor models.[51,52] Lymphoid organogenesis is initiated by the cross-talk of LTβR-expressing mesenchymal lymphoid tissue organizer (LTo) cells and hematopoietic $LT\alpha1\beta2$-expressing LTi cells.[10,53,54] Recent studies on TLLSs revealed cancer-associated fibroblasts (CAFs) as surrogate LTo cells and CD8 T cells and $LT\alpha1\beta2^+$ B cells as LTi cells.[53] Although HEV formation in SLOs is not fully understood,[55] $LT\alpha1\beta2$-producing $CD11c^+$ DCs are required for HEV formation and LN homeostasis.[22,38] CD11c, considered a pan-DC marker, is commonly expressed in TAMs.[56] We observed few DCs and many $CD11c^+$ macrophages in HEV^+ tumors. Although TAM or CD4 T cell depletion

(C) Digital reconstruction of a representative human breast cancer section by MILAN. The selected area depicts HEV high area (with >25% HEV-ECs) or HEV low area (with <25% HEV-ECs) at tumor edge/bulk. Scale bar indicates 2 mm. Scale bars in the selections indicate 50 μm.
(D) CD8 T cells numbers in distinct human breast cancer locations.
(E) Density plot depicting the distance between each indicated CD8 T cell subset to the closest HEV or blood vessels (BV).
(F) Illustration of CD8 T cell subsets in the TU-HEV niche.
(G and H) GSVA score of the human HEV signature in melanoma patients (CA209-038) from samples collected before (Pre) or during (On) immunotherapy (G), and NSCLC patients before anti-PD-L1 therapy (atezolizumab) from the Poplar study (H).
Median-quantile-min/max without outliers ± population distribution is shown in violin ± boxplot (A, B, D, G, and H). Mouse data are derived from four MC38 tumors treated with anti-CTLA-4 and LTβR agonist (both from Oncurious). Human data are derived from five to six human untreated breast cancers. Wilcoxon test with the adjusted p value using Holm correction (A and D) or without p value adjustment (G). *$p < 0.05$; **$p < 0.01$; ***$p < 0.001$; ****$p < 0.0001$. CR, complete responder; PD, progression disease; PR, partial responder; SD, stable disease. See also Figure S7.

did not impair TU-HEV formation during antiangiogenic immunotherapy, the lack of CD8 T cells and NK cells did. Similar results were observed with spontaneously arising HEVs in murine tumors.[39] Importantly, the degree of HEV impairment directly correlated with the apoptotic index and anti-tumor effect, rendering antiangiogenic ICB therapy nearly completely ineffective in the absence of NK plus CD8 T cells. Congruently, NK and CD8 T cells expressed the highest levels of LTα and LTβ among other immune cell constituents, and EC-specific genetic deletion of the LTβR severely reduced TU-HEVs in ICB-treated tumors, revealing the LTβR axis as a critical regulator for the acquisition of mature TU-HEV formation. The few observed immature TU-HEVs derived from LTβR-deficient ECs may have likely been generated by LTα3/TNFR signaling because this pathway is upregulated during inflammation and found to induce immature MECA79$^+$.[39] Notably, IFNγ did not impact the therapeutic induction of HEVs, but it induced an inflammation response with increased SelE and SelP that retain activated lymphocytes. It is therefore conceivable that IFNγ raises the threshold of lymphocyte infiltrates and may, as such, contribute to the formation of spontaneous HEVs.

How do TU-ECs then develop into HEVs? TU-HEVs preferentially appear as hotspots close to the tumor rim, which is suggestive of specific vascular locations and ECs from which HEVs can arise. Intravital imaging of inflamed LNs displayed clonal proliferation of HEV cells that acted as local progenitors to generate capillaries and HEV neovessels.[57] Recent scRNA-seq and genetic lineage tracing of the LN vasculature identified a primed capillary resident regenerative population (CRP) that may function as progenitors of the blood vascular endothelium, including HEVs in LNs.[27] We demonstrated that TU-HEVs were not generated from a specific endothelial progenitor population by clonal expansion but rather by metaplasia from a common population of PCVs. PCV conversion into HEVs occurred within days of antiangiogenic immunotherapy and promptly reverted after therapy termination. The observation that lymphoid-derived signals promote PCV specialization to HEVs, boosting lymphocyte infiltration, and require continuous signals to maintain this specialized state sets the stage for novel therapeutic opportunities that controllably induce HEVs and subsequent TCF1$^+$ CD8 T cell-containing TA-TLLSs to improve current immunotherapies.

STAR★METHODS

Detailed methods are provided in the online version of this paper and include the following:

- KEY RESOURCES TABLE
- RESOURCE AVAILABILITY
  - Lead contact
  - Materials availability
  - Data and code availability
- EXPERIMENTAL MODEL AND SUBJECT DETAILS
  - Cell lines
  - Animal strains
  - Human samples
- METHOD DETAILS
  - Mouse trials
  - Tissue dissociation and sample preparation
  - Flow cytometry
  - Gene expression analysis
  - Immunostaining
  - MILAN multiplex immunohistochemistry
  - Single-cell RNA sequencing
  - Single-cell transcriptomics analysis
  - Bulk RNA sequencing analysis
- QUANTIFICATION AND STATISTICAL ANALYSIS

SUPPLEMENTAL INFORMATION

Supplemental information can be found online at https://doi.org/10.1016/j.ccell.2022.11.002.

ACKNOWLEDGMENTS

This work is dedicated to the late Dr. Zena Werb. We thank Dr. E. Butcher for insightful discussion and Dr. J. Browning (Boston University) for the mouse LTβR-Ig Fusion protein. At VIB- KU Leuven, we thank K. Feyen and N. Dupont for their technical assistance, P. Zhao and Dr. J. Poźniak for assistance with the scRNA-seq analysis, the VIB histology core for histology assistance, the VIB Bio Imaging Core for microscopy assistance, S. Vlayen for administrative and logistical support, and the KU Leuven FACS core and Dr. O. Burton (University of Cambridge) for assistance with flow cytometry. We thank Dr. P. Boström and Dr. I. Koskivuo (both Turku University Hospital) for helping with patient sample acquisition. This work was supported by grants from the Flemish government FWO (G0A0818N to G.B.); the National Institutes of Health, National Cancer Institute (NIH/NCI; R01CA201537 to G.B.); the Kom op tegen Kanker, Emmanuel van der Schueren starter fellowship (2018/11321/2822 to Y.H.); the Academy of Finland; the Finnish Cancer Foundation; the Jane and Aatos Erkko Foundation; and the Sigrid Jusélius Foundation.

AUTHOR CONTRIBUTIONS

Y.H., G.V., S.S., and G.B. designed experiments; Y.H., G.V., E.A., D.N., Steffie Junius, and M.D. performed all experiments unless specified; A.S., S.D., T.H., G.F., P.M., Damya Laoui, Diether Lambrechts, and A.L. provided and generated critical reagents, software, and input; A.A.M. and F.M.B. analyzed MILAN multiplex immunohistochemistry; A.T., Sirpa Jalkanen, and M.H. provided the human breast cancer tissues for the MILAN multiplex immunohistochemistry; G.B., S.S., and F.R. conceptually planned and supervised the study; G.B. wrote the manuscript; and Y.H., G.V., S.S., and F.R. edited the manuscript.

DECLARATION OF INTERESTS

G.B. has received research funding from Oncurious NV and is listed as an inventor on patent applications filed by Oncurious NV related to the subject matter of this work. The other authors declare no competing interests.

Received: December 23, 2021
Revised: July 20, 2022
Accepted: November 4, 2022
Published: November 23, 2022

REFERENCES

1. Hodi, F.S., O'Day, S.J., McDermott, D.F., Weber, R.W., Sosman, J.A., Haanen, J.B., Gonzalez, R., Robert, C., Schadendorf, D., Hassel, J.C., et al. (2010). Improved survival with ipilimumab in patients with metastatic melanoma. N. Engl. J. Med. *363*, 711–723. https://doi.org/10.1056/NEJMoa1003466.
2. Topalian, S.L., Hodi, F.S., Brahmer, J.R., Gettinger, S.N., Smith, D.C., McDermott, D.F., Powderly, J.D., Carvajal, R.D., Sosman, J.A., Atkins, M.B., et al. (2012). Safety, activity, and immune correlates of anti-PD-1

antibody in cancer. N. Engl. J. Med. *366*, 2443–2454. https://doi.org/10.1056/NEJMoa1200690.

3. Anandappa, A.J., Wu, C.J., and Ott, P.A. (2020). Directing traffic: how to effectively drive T cells into tumors. Cancer Discov. *10*, 185–197. https://doi.org/10.1158/2159-8290.CD-19-0790.
4. Ayers, M., Lunceford, J., Nebozhyn, M., Murphy, E., Loboda, A., Kaufman, D.R., Albright, A., Cheng, J.D., Kang, S.P., Shankaran, V., et al. (2017). IFN-gamma-related mRNA profile predicts clinical response to PD-1 blockade. J. Clin. Invest. *127*, 2930–2940. https://doi.org/10.1172/JCI91190.
5. Schumacher, T.N., and Schreiber, R.D. (2015). Neoantigens in cancer immunotherapy. Science *348*, 69–74. https://doi.org/10.1126/science.aaa4971.
6. Tumeh, P.C., Harview, C.L., Yearley, J.H., Shintaku, I.P., Taylor, E.J.M., Robert, L., Chmielowski, B., Spasic, M., Henry, G., Ciobanu, V., et al. (2014). PD-1 blockade induces responses by inhibiting adaptive immune resistance. Nature *515*, 568–571. https://doi.org/10.1038/nature13954.
7. Jansen, C.S., Prokhnevska, N., Master, V.A., Sanda, M.G., Carlisle, J.W., Bilen, M.A., Cardenas, M., Wilkinson, S., Lake, R., Sowalsky, A.G., et al. (2019). An intra-tumoral niche maintains and differentiates stem-like CD8 T cells. Nature *576*, 465–470. https://doi.org/10.1038/s41586-019-1836-5.
8. Kurtulus, S., Madi, A., Escobar, G., Klapholz, M., Nyman, J., Christian, E., Pawlak, M., Dionne, D., Xia, J., Rozenblatt-Rosen, O., et al. (2019). Checkpoint blockade immunotherapy induces dynamic changes in PD-1(-)CD8(+) tumor-infiltrating T cells. Immunity *50*, 181–194.e6. https://doi.org/10.1016/j.immuni.2018.11.014.
9. Siddiqui, I., Schaeuble, K., Chennupati, V., Fuertes Marraco, S.A., Calderon-Copete, S., Pais Ferreira, D., Carmona, S.J., Scarpellino, L., Gfeller, D., Pradervand, S., et al. (2019). Intratumoral tcf1(+)PD-1(+)CD8(+) T cells with stem-like properties promote tumor control in response to vaccination and checkpoint blockade immunotherapy. Immunity *50*, 195–211.e10. https://doi.org/10.1016/j.immuni.2018.12.021.
10. Sautès-Fridman, C., Petitprez, F., Calderaro, J., and Fridman, W.H. (2019). Tertiary lymphoid structures in the era of cancer immunotherapy. Nat. Rev. Cancer *19*, 307–325. https://doi.org/10.1038/s41568-019-0144-6.
11. Gago da Graça, C., van Baarsen, L.G.M., and Mebius, R.E. (2021). Tertiary lymphoid structures: diversity in their development, composition, and role. J. Immunol. *206*, 273–281. https://doi.org/10.4049/jimmunol.2000873.
12. Neyt, K., Perros, F., GeurtsvanKessel, C.H., Hammad, H., and Lambrecht, B.N. (2012). Tertiary lymphoid organs in infection and autoimmunity. Trends Immunol. *33*, 297–305. https://doi.org/10.1016/j.it.2012.04.006.
13. Motz, G.T., Santoro, S.P., Wang, L.P., Garrabrant, T., Lastra, R.R., Hagemann, I.S., Lal, P., Feldman, M.D., Benencia, F., and Coukos, G. (2014). Tumor endothelium FasL establishes a selective immune barrier promoting tolerance in tumors. Nat. Med. *20*, 607–615. https://doi.org/10.1038/nm.3541.
14. He, B., Jabouille, A., Steri, V., Johansson-Percival, A., Michael, I.P., Kotamraju, V.R., Junckerstorff, R., Nowak, A.K., Hamzah, J., Lee, G., et al. (2018). Vascular targeting of LIGHT normalizes blood vessels in primary brain cancer and induces intratumoural high endothelial venules. J. Pathol. *245*, 209–221. https://doi.org/10.1002/path.5080.
15. Jain, R.K. (2001). Normalizing tumor vasculature with anti-angiogenic therapy: a new paradigm for combination therapy. Nat. Med. *7*, 987–989. https://doi.org/10.1038/nm0901-987.
16. Rivera, L.B., and Bergers, G. (2015). Intertwined regulation of angiogenesis and immunity by myeloid cells. Trends Immunol. *36*, 240–249. https://doi.org/10.1016/j.it.2015.02.005.
17. Schmittnaegel, M., Rigamonti, N., Kadioglu, E., Cassará, A., Wyser Rmili, C., Kiialainen, A., Kienast, Y., Mueller, H.J., Ooi, C.H., Laoui, D., and De Palma, M. (2017). Dual angiopoietin-2 and VEGFA inhibition elicits antitumor immunity that is enhanced by PD-1 checkpoint blockade. Sci. Transl. Med. *9*, eaak9670. https://doi.org/10.1126/scitranslmed.aak9670.
18. Allen, E., Jabouille, A., Rivera, L.B., Lodewijckx, I., Missiaen, R., Steri, V., Feyen, K., Tawney, J., Hanahan, D., Michael, I.P., and Bergers, G. (2017). Combined antiangiogenic and anti-PD-L1 therapy stimulates tumor immunity through HEV formation. Sci. Transl. Med. *9*, eaak9679. https://doi.org/10.1126/scitranslmed.aak9679.
19. Martinet, L., Garrido, I., Filleron, T., Le Guellec, S., Bellard, E., Fournie, J.J., Rochaix, P., and Girard, J.P. (2011). Human solid tumors contain high endothelial venules: association with T- and B-lymphocyte infiltration and favorable prognosis in breast cancer. Cancer Res. *71*, 5678–5687. https://doi.org/10.1158/0008-5472.Can-11-0431.
20. Vella, G., Guelfi, S., and Bergers, G. (2021). High endothelial venules: a vascular perspective on tertiary lymphoid structures in cancer. Front. Immunol. *12*, 736670. https://doi.org/10.3389/fimmu.2021.736670.
21. Homeister, J.W., Thall, A.D., Petryniak, B., Malý, P., Rogers, C.E., Smith, P.L., Kelly, R.J., Gersten, K.M., Askari, S.W., Cheng, G., et al. (2001). The alpha(1, 3)fucosyltransferases FucT-IV and FucT-VII exert collaborative control over selectin-dependent leukocyte recruitment and lymphocyte homing. Immunity *15*, 115–126. https://doi.org/10.1016/s1074-7613(01)00166-2.
22. Girard, J.P., Moussion, C., and Förster, R. (2012). HEVs, lymphatics and homeostatic immune cell trafficking in lymph nodes. Nat. Rev. Immunol. *12*, 762–773. https://doi.org/10.1038/nri3298.
23. Rosen, S.D. (2004). Ligands for L-selectin: homing, inflammation, and beyond. Annu. Rev. Immunol. *22*, 129–156. https://doi.org/10.1146/annurev.immunol.21.090501.080131.
24. Malý, P., Thall, A., Petryniak, B., Rogers, C.E., Smith, P.L., Marks, R.M., Kelly, R.J., Gersten, K.M., Cheng, G., Saunders, T.L., et al. (1996). The alpha(1, 3)fucosyltransferase Fuc-TVII controls leukocyte trafficking through an essential role in L-E-and P-selectin ligand biosynthesis. Cell *86*, 643–653. https://doi.org/10.1016/s0092-8674(00)80137-3.
25. Streeter, P.R., Rouse, B.T., and Butcher, E.C. (1988). Immunohistologic and functional characterization of a vascular addressin involved in lymphocyte homing into peripheral lymph nodes. J. Cell Biol. *107*, 1853–1862. https://doi.org/10.1083/jcb.107.5.1853.
26. Veerman, K., Tardiveau, C., Martins, F., Coudert, J., and Girard, J.P. (2019). Single-cell analysis reveals heterogeneity of high endothelial venules and different regulation of genes controlling lymphocyte entry to lymph nodes. Cell Rep. *26*, 3116–3131.e5. https://doi.org/10.1016/j.celrep.2019.02.042.
27. Brulois, K., Rajaraman, A., Szade, A., Nordling, S., Bogoslowski, A., Dermadi, D., Rahman, M., Kiefel, H., O'Hara, E., Koning, J.J., et al. (2020). A molecular map of murine lymph node blood vascular endothelium at single cell resolution. Nat. Commun. *11*, 3798. https://doi.org/10.1038/s41467-020-17291-5.
28. Aibar, S., González-Blas, C.B., Moerman, T., Huynh-Thu, V.A., Imrichova, H., Hulselmans, G., Rambow, F., Marine, J.C., Geurts, P., Aerts, J., et al. (2017). SCENIC: single-cell regulatory network inference and clustering. Nat. Methods *14*, 1083–1086. https://doi.org/10.1038/nmeth.4463.
29. Goveia, J., Rohlenova, K., Taverna, F., Treps, L., Conradi, L.C., Pircher, A., Geldhof, V., de Rooij, L.P.M.H., Kalucka, J., Sokol, L., et al. (2020). An integrated gene expression landscape profiling approach to identify lung tumor endothelial cell heterogeneity and angiogenic candidates. Cancer Cell *37*, 421. https://doi.org/10.1016/j.ccell.2020.03.002.
30. Melrose, J., Tsurushita, N., Liu, G., and Berg, E.L. (1998). IFN-gamma inhibits activation-induced expression of E- and P-selectin on endothelial cells. J. Immunol. *161*, 2457–2464.
31. Bassez, A., Vos, H., Van Dyck, L., Floris, G., Arijs, I., Desmedt, C., Boeckx, B., Vanden Bempt, M., Nevelsteen, I., Lambein, K., et al. (2021). A single-cell map of intratumoral changes during anti-PD1 treatment of patients with breast cancer. Nat. Med. *27*, 820–832. https://doi.org/10.1038/s41591-021-01323-8.
32. Setty, M., Kiseliovas, V., Levine, J., Gayoso, A., Mazutis, L., and Pe'er, D. (2019). Characterization of cell fate probabilities in single-cell data with Palantir. Nat. Biotechnol. *37*, 451–460. https://doi.org/10.1038/s41587-019-0068-4.
33. Bergen, V., Lange, M., Peidli, S., Wolf, F.A., and Theis, F.J. (2020). Generalizing RNA velocity to transient cell states through dynamical

modeling. Nat. Biotechnol. *38*, 1408–1414. https://doi.org/10.1038/s41587-020-0591-3.

34. La Manno, G., Soldatov, R., Zeisel, A., Braun, E., Hochgerner, H., Petukhov, V., Lidschreiber, K., Kastriti, M.E., Lönnerberg, P., Furlan, A., et al. (2018). RNA velocity of single cells. Nature *560*, 494–498. https://doi.org/10.1038/s41586-018-0414-6.

35. Manavski, Y., Lucas, T., Glaser, S.F., Dorsheimer, L., Günther, S., Braun, T., Rieger, M.A., Zeiher, A.M., Boon, R.A., and Dimmeler, S. (2018). Clonal expansion of endothelial cells contributes to ischemia-induced neovascularization. Circ. Res. *122*, 670–677. https://doi.org/10.1161/CIRCRESAHA.117.312310.

36. Colbeck, E.J., Jones, E., Hindley, J.P., Smart, K., Schulz, R., Browne, M., Cutting, S., Williams, A., Parry, L., Godkin, A., et al. (2017). Treg depletion licenses T cell-driven HEV neogenesis and promotes tumor destruction. Cancer Immunol. Res. *5*, 1005–1015. https://doi.org/10.1158/2326-6066.Cir-17-0131.

37. Johansson-Percival, A., He, B., Li, Z.J., Kjellén, A., Russell, K., Li, J., Larma, I., and Ganss, R. (2017). De novo induction of intratumoral lymphoid structures and vessel normalization enhances immunotherapy in resistant tumors. Nat. Immunol. *18*, 1207–1217. https://doi.org/10.1038/ni.3836.

38. Moussion, C., and Girard, J.P. (2011). Dendritic cells control lymphocyte entry to lymph nodes through high endothelial venules. Nature *479*, 542–546. https://doi.org/10.1038/nature10540.

39. Peske, J.D., Thompson, E.D., Gemta, L., Baylis, R.A., Fu, Y.X., and Engelhard, V.H. (2015). Effector lymphocyte-induced lymph node-like vasculature enables naive T-cell entry into tumours and enhanced anti-tumour immunity. Nat. Commun. *6*, 7114. https://doi.org/10.1038/ncomms8114.

40. van de Pavert, S.A., and Mebius, R.E. (2010). New insights into the development of lymphoid tissues. Nat. Rev. Immunol. *10*, 664–674. https://doi.org/10.1038/nri2832.

41. Browaeys, R., Saelens, W., and Saeys, Y. (2020). NicheNet: modeling intercellular communication by linking ligands to target genes. Nat. Methods *17*, 159–162. https://doi.org/10.1038/s41592-019-0667-5.

42. Spranger, S., and Gajewski, T.F. (2015). A new paradigm for tumor immune escape: beta-catenin-driven immune exclusion. J. Immunother. Cancer *3*, 43. https://doi.org/10.1186/s40425-015-0089-6.

43. Miller, B.C., Sen, D.R., Al Abosy, R., Bi, K., Virkud, Y.V., LaFleur, M.W., Yates, K.B., Lako, A., Felt, K., Naik, G.S., et al. (2019). Subsets of exhausted CD8(+) T cells differentially mediate tumor control and respond to checkpoint blockade. Nat. Immunol. *20*, 326–336. https://doi.org/10.1038/s41590-019-0312-6.

44. Bolognesi, M.M., Manzoni, M., Scalia, C.R., Zannella, S., Bosisio, F.M., Faretta, M., and Cattoretti, G. (2017). Multiplex staining by sequential immunostaining and antibody removal on routine tissue sections. J. Histochem. Cytochem. *65*, 431–444. https://doi.org/10.1369/0022155417719419.

45. Riaz, N., Havel, J.J., Makarov, V., Desrichard, A., Urba, W.J., Sims, J.S., Hodi, F.S., Martín-Algarra, S., Mandal, R., Sharfman, W.H., et al. (2017). Tumor and microenvironment evolution during immunotherapy with nivolumab. Cell *171*, 934–949.e16. https://doi.org/10.1016/j.cell.2017.09.028.

46. Fehrenbacher, L., Spira, A., Ballinger, M., Kowanetz, M., Vansteenkiste, J., Mazieres, J., Park, K., Smith, D., Artal-Cortes, A., Lewanski, C., et al. (2016). Atezolizumab versus docetaxel for patients with previously treated non-small-cell lung cancer (POPLAR): a multicentre, open-label, phase 2 randomised controlled trial. Lancet *387*, 1837–1846. https://doi.org/10.1016/s0140-6736(16)00587-0.

47. Banchereau, R., Leng, N., Zill, O., Sokol, E., Liu, G., Pavlick, D., Maund, S., Liu, L.-F., Kadel, E., 3rd, Baldwin, N., et al. (2021). Molecular determinants of response to PD-L1 blockade across tumor types. Nat. Commun. *12*, 3969. https://doi.org/10.1038/s41467-021-24112-w.

48. Herbst, R.S., Soria, J.C., Kowanetz, M., Fine, G.D., Hamid, O., Gordon, M.S., Sosman, J.A., McDermott, D.F., Powderly, J.D., Gettinger, S.N., et al. (2014). Predictive correlates of response to the anti-PD-L1 antibody MPDL3280A in cancer patients. Nature *515*, 563–567. https://doi.org/10.1038/nature14011.

49. Asrir, A., Tardiveau, C., Coudert, J., Laffont, R., Blanchard, L., Bellard, E., Veerman, K., Bettini, S., Lafouresse, F., Vina, E., et al. (2022). Tumor-associated high endothelial venules mediate lymphocyte entry into tumors and predict response to PD-1 plus CTLA-4 combination immunotherapy. Cancer Cell *40*, 318–334.e9. https://doi.org/10.1016/j.ccell.2022.01.002.

50. Johansson-Percival, A., Li, Z.J., Lakhiani, D.D., He, B., Wang, X., Hamzah, J., and Ganss, R. (2015). Intratumoral LIGHT restores pericyte contractile properties and vessel integrity. Cell Rep. *13*, 2687–2698. https://doi.org/10.1016/j.celrep.2015.12.004.

51. Lauder, S.N., Smart, K., Kersemans, V., Allen, D., Scott, J., Pires, A., Milutinovic, S., Somerville, M., Smart, S., Kinchesh, P., et al. (2020). Enhanced antitumor immunity through sequential targeting of PI3Kδ and LAG3. J. Immunother. Cancer *8*, e000693. https://doi.org/10.1136/jitc-2020-000693.

52. He, T., Hao, Z., Lin, M., Xin, Z., Chen, Y., Ouyang, W., Yang, Q., Chen, X., Zhou, H., Zhang, W., et al. (2022). Oncolytic adenovirus promotes vascular normalization and nonclassical tertiary lymphoid structure formation through STING-mediated DC activation. OncoImmunology *11*, 2093054. https://doi.org/10.1080/2162402x.2022.2093054.

53. Rodriguez, A.B., Peske, J.D., Woods, A.N., Leick, K.M., Mauldin, I.S., Meneveau, M.O., Young, S.J., Lindsay, R.S., Melssen, M.M., Cyranowski, S., et al. (2021). Immune mechanisms orchestrate tertiary lymphoid structures in tumors via cancer-associated fibroblasts. Cell Rep. *36*, 109422. https://doi.org/10.1016/j.celrep.2021.109422.

54. Johansson-Percival, A., and Ganss, R. (2021). Therapeutic induction of tertiary lymphoid structures in cancer through stromal remodeling. Front. Immunol. *12*, 674375. https://doi.org/10.3389/fimmu.2021.674375.

55. Ager, A. (2017). High endothelial venules and other blood vessels: critical regulators of lymphoid organ development and function. Front. Immunol. *8*, 45. https://doi.org/10.3389/fimmu.2017.00045.

56. Gautier, E.L., Shay, T., Miller, J., Greter, M., Jakubzick, C., Ivanov, S., Helft, J., Chow, A., Elpek, K.G., Gordonov, S., et al. (2012). Gene-expression profiles and transcriptional regulatory pathways that underlie the identity and diversity of mouse tissue macrophages. Nat. Immunol. *13*, 1118–1128. https://doi.org/10.1038/ni.2419.

57. Mondor, I., Jorquera, A., Sene, C., Adriouch, S., Adams, R.H., Zhou, B., Wienert, S., Klauschen, F., and Bajénoff, M. (2016). Clonal proliferation and stochastic pruning orchestrate lymph node vasculature remodeling. Immunity *45*, 877–888. https://doi.org/10.1016/j.immuni.2016.09.017.

58. Ouyang, J.F., Kamaraj, U.S., Cao, E.Y., and Rackham, O.J.L. (2021). ShinyCell: simple and sharable visualisation of single-cell gene expression data. Bioinformatics *37*, 3374–3376. https://doi.org/10.1093/bioinformatics/btab209.

59. Bosisio, F.M., Antoranz, A., van Herck, Y., Bolognesi, M.M., Marcelis, L., Chinello, C., Wouters, J., Magni, F., Alexopoulos, L., Stas, M., et al. (2020). Functional heterogeneity of lymphocytic patterns in primary melanoma dissected through single-cell multiplexing. Elife *9*, e53008. https://doi.org/10.7554/eLife.53008.

60. Giorgio, C., Francesca Maria, B., Lukas, M., and Maddalena Maria, B. (2021). Protocol Exchange. https://doi.org/10.21203/rs.2.1646/v5.

61. Matungka, R., Zheng, Y.F., and Ewing, R.L. (2009). Image registration using adaptive polar transform. IEEE Trans. Image Process. *18*, 2340–2354. https://doi.org/10.1109/TIP.2009.2025010.

62. Schmidt, U., Weigert, M., Broaddus, C., and Myers, G. (2018). Cell Detection with Star-Convex Polygons. Held in Cham (Springer International Publishing), pp. 265–273.

63. Picelli, S., Faridani, O.R., Björklund, A.K., Winberg, G., Sagasser, S., and Sandberg, R. (2014). Full-length RNA-seq from single cells using Smart-seq2. Nat. Protoc. *9*, 171–181. https://doi.org/10.1038/nprot.2014.006.

64. Stuart, T., Butler, A., Hoffman, P., Hafemeister, C., Papalexi, E., Mauck, W.M., 3rd, Hao, Y., Stoeckius, M., Smibert, P., and Satija, R. (2019). Comprehensive integration of single-cell data. Cell *177*, 1888–1902.e21. https://doi.org/10.1016/j.cell.2019.05.031.

65. van der Maaten, L., and Hinton, G. (2012). Visualizing non-metric similarities in multiple maps. Mach. Learn. *87*, 33–55. https://doi.org/10.1007/s10994-011-5273-4.

66. Shannon, P., Markiel, A., Ozier, O., Baliga, N.S., Wang, J.T., Ramage, D., Amin, N., Schwikowski, B., and Ideker, T. (2003). Cytoscape: a software environment for integrated models of biomolecular interaction networks. Genome Res. *13*, 2498–2504. https://doi.org/10.1101/gr.1239303.

67. Gulati, G.S., Sikandar, S.S., Wesche, D.J., Manjunath, A., Bharadwaj, A., Berger, M.J., Ilagan, F., Kuo, A.H., Hsieh, R.W., Cai, S., et al. (2020). Single-cell transcriptional diversity is a hallmark of developmental potential. Science *367*, 405–411. https://doi.org/10.1126/science.aax0249.

68. Bankhead, P., Loughrey, M.B., Fernández, J.A., Dombrowski, Y., McArt, D.G., Dunne, P.D., McQuaid, S., Gray, R.T., Murray, L.J., Coleman, H.G., et al. (2017). QuPath: open source software for digital pathology image analysis. Sci. Rep. *7*, 16878. https://doi.org/10.1038/s41598-017-17204-5.

STAR★METHODS

KEY RESOURCES TABLE

REAGENT or RESOURCE	SOURCE	IDENTIFIER
Antibodies		
AF647 anti-mouse/human CD45R/B220	Biolegend	Cat# 103226; RRID: AB_389330
Rabbit anti-CD31 (polyclonal)	Abcam	Cat# ab28364; RRID: AB_726362
Anti-PECAM-1 (CD31) (2H8)	Sigma	Cat# MAB1398Z; RRID: AB_94207
APC anti-mouse CD31 (390)	Biolegend	Cat# 102410; RRID: AB_312905
anti-human PECAM-1/CD31 Antibody (OTI2C6)	LSBio	Cat# LS-B16850
Purified Hamster Anti-Mouse CD54 (ICAM-1) (3E2)	BD Biosciences	Cat# 550287; RRID: AB_393582
AF488 anti-mouse/human High Endothelial Venule Marker (MECA-79)	Invitrogen	Cat# 53-6036-82; RRID: AB_10804391
AF647 anti-mouse/human PNAd Antibody (MECA-79)	Biolegend	Cat# 120808; RRID: AB_2783060
AF488 Anti-MECA-79 (MECA-79)	Santa Cruz Biotechnology	Cat# sc-19602 AF488; RRID: AB_627143
Purified Rat Anti-Mouse CD62E (SelectinE) (10E9.6)	BD Biosciences	Cat# 553749; RRID: AB_2186705
AF647 Anti-Mouse CD62P (SelectinP) (RB40.34)	BD Biosciences	Cat# 563674; RRID: AB_2738366
Anti-mouse CD106 (VCAM-1) (429)	Invitrogen	Cat# 14-1061-82; RRID: AB_467419
Anti-mouse/human von Willebrand factor (vWf) (polyclonal)	Dako	Cat# A0082; RRID: AB_2315602
APC anti-mouse CD8a (53–6.7)	Biolegend	Cat# 100712; RRID: AB_312751
BUV805 anti-mouse CD8a (53–6.7)	BD Biosciences	Cat# 564920; RRID: AB_2716856
BV421 anti-mouse CD8a (53–6.7)	Biolegend	Cat# 100737; RRID: AB_10897101
Anti-mouse CD8a (4SM15)	Invitrogen	Cat# 14-0808-82; RRID: AB_2572861
Anti-CD8a Antibody (C8/144B)	Santa Cruz	Cat# sc-53212; RRID: AB_1120718
AF647 anti-mouse CD4 (RM4-5)	Biolegend	Cat# 100530; RRID: AB_389325
BUV496 anti-mouse CD4 (GK1.5)	BD Biosciences	Cat# 564667; RRID: AB_2722549
BV510 anti-mouse/human CD11b (M1/70)	Biolegend	Cat# 101263; RRID: AB_2629529
BV750 anti-mouse/human CD11b (M1/70)	BD Biosciences	Special order
PE-Dazzle 594 anti-mouse CD64 (FcγRI) (X54-5/7.1)	Biolegend	Cat# 139320; RRID: AB_2566559
BV650 anti-mouse CD3 (17A2)	Biolegend	Cat# 100229; RRID: AB_11204249
BV570 anti-mouse CD3 (17A2)	Biolegend	Cat# 100225; RRID: AB_10900444
APC anti-mouse CD3 (17A2)	Biolegend	Cat# 100236; RRID: AB_2561456
BUV563 anti-mouse Ly6C (HK1.4)	BD Biosciences	Special order
PE/Cy7 anti-mouse LTβR (5G11)	Biolegend	Cat# 134409; RRID:AB_2728152
PE/Cyanine7 anti-mouse CD172a (SIRPa) (P84)	Biolegend	Cat# 144008; RRID: AB_2563546
APC anti-mouse FOXP3 (REA788)	Miltenyi Biotec	Cat# 130-111-601; RRID: AB_2651768
FOXP3 Monoclonal Antibody Biotin (FJK-16s)	eBioscience	Cat# 13-5773-82; RRID: AB_763540
APC anti-mouse CD45 (30-F11)	Biolegend	Cat# 103112; RRID: AB_312977
BUV395 Anti-Mouse CD45 (30-F11)	BD Bioscience	Cat# 565967; RRID: AB_2739420
PE anti-mouse Granzyme B (NGZB)	eBioscience	Cat# 12-8898-82; RRID: AB_10870787
PE/Dazzle 594 anti-human/mouse Granzyme B (QA16A02)	Biolegend	Cat# 372215; RRID: AB_2728382
Anti-mouse Granzyme B Biotinylated (polyclonal)	R&D	Cat# BAF1865; RRID: AB_2114416
BV711 anti-mouse CD279 (PD1) (29F.1A12)	Biolegend	Cat# 135231; RRID: AB_2566158
Anti-human PD-1 (D4W2J) 86163	Cell Signaling	Cat# 86163; RRID: AB_2728833
AF555 anti-mouse PD-1 (D7D5W)	Cell Signaling	Cat# 76733; RRID: AB_2799886
Mouse PD-1 Antibody (polyclonal)	R&D	Cat# AF1021; RRID: AB_354541
BV421 anti-mouse CD11c (N418)	Biolegend	Cat# 117330; RRID: AB_11219593

(*Continued on next page*)

Continued

REAGENT or RESOURCE	SOURCE	IDENTIFIER
Purified anti-mouse NK-1.1 Antibody (PK136)	Biolegend	Cat# 108702; RRID: AB_313389
BB630 anti-mouse T-bet (4B10)	BD Biosciences	Special order
AF700 anti-mouse I-A/I-E (MHC-II) (M5/114.15.2)	Biolegend	Cat# 107622; RRID:AB_493727
BV570 anti-mouse Ly6G (1A8)	Biolegend	Cat# 127629; RRID: AB_10899738
BV570 anti-mouse/human CD44 (IM7)	Biolegend	Cat# 103037; RRID: AB_10900641
APC/Fire 750 anti-mouse/human CD44 (IM7)	Biolegend	Cat# 103061; RRID: AB_2616726
BUV737 anti-mouse IFN-γ (XMG1.2)	BD Biosciences	Cat# 564693; RRID: AB_2722494
PE anti-mouse RORγT (B2D)	eBioscience	Cat# 12-6981-80; RRID: AB_10805392
PerCP-Vio700 anti-mouse CD317 (PDCA-1) (REA818)	Miltenyi Biotec	Cat# 130-112-224; RRID: AB_2657408
BV480 anti-mouse CD25 (PC61)	BD Biosciences	Cat# 566120; RRID: AB_2739522
BV605 Anti-mouse CD366 (TIM-3) (RMT3-23)	Biolegend	Cat# 119721; RRID: AB_2616907
TIM-3 Rabbit mAb (E9K5D)	Cell Signaling	Cat# 75743
Recombinant Anti-TIM 3 antibody (EPR22241)	Abcam	Cat# ab241332; RRID: AB_2888936
Anti-human TIM-3 (polyclonal)	R&D	Cat # AF2365; RRID: AB_355235
Pe-Cy7 TCF1/TCF7 (C63D9)	Cell signaling	Cat# 90511
Anti-Mouse TCF1 (C63D9)	Cell signaling	Cat# 2203T; RRID: AB_2199302
BV650 anti-mouse XCR1 (ZET)	Biolegend	Cat# 148220; RRID: AB_2566410
BUV661 anti-mouse CD127 (SB/199)	BD Biosciences	Cat# 624285
AF700 anti-mouse Ki-67 (16A8)	Biolegend	Cat# 652419; RRID: AB_2564284
AF488 anti-mouse Ki-67 (D3B5)	Cell Signaling	Cat# 11882; RRID: AB_2687824
Anti-human Ki-67 (UMAB107)	Origene	Cat# UM800033; RRID: AB_2629145
PE/Cy5 anti-mouse TCR β chain (H57-597)	Biolegend	Cat# 109209; RRID: AB_313432
BV785 anti-mouse CD19 (1D3;B4)	Biolegend	Cat# 115543; RRID: AB_11218994
BV421 anti-mouseTNF-α (MP6-XT22)	Biolegend	Cat# 506328; RRID: AB_2562902
Anti-human/mouse desmin (polyclonal)	R&D	Cat# AF3844; RRID: AB_2092419
Anti-human Perforin (5B10)	Abcam	Cat# ab89821; RRID: AB_2042606
Purified Rat Anti-Mouse CD16/CD32 (Fc Block)	BD Biosciences	Cat# 553142; RRID: AB_394657
InVivoMAb anti-mouse CSF1R (CD115)	BioXCell	Cat# BE0213; RRID: AB_2687699
InVivoMAb anti-mouse CD4	BioXCell	Cat# BE0003-1; RRID: AB_1107636
InVivoMAb anti-mouse CD8	BioXCell	Cat# BE0061; RRID: AB_1125541
InVivoMab rat IgG2b isotype control	BioXCell	Cat# BE0090; RRID: AB_1107780
InVivoMAb anti-mouse NK1.1	BioXCell	Cat# BE0036; RRID: AB_1107737
InVivoMAb anti-mouse IFNγ	BioXCell	Cat# BE0055; RRID: AB_1107694
InVivoMAb anti-mouse VEGFR-2 (DC101)	BioXCell	Cat# BE0060; RRID: AB_1107766
InVivoMAb anti-mouse PD-L1 (B7-H1)	BioXCell	Cat# BE0101; RRID: AB_10949073
InVivoMAb anti-mouse CTLA-4 (CD152)	BioXCell	Cat# BE0164; RRID: AB_10949609
Lymphotoxin Beta Receptor antibody (5G11b)	Biorad	Cat# MCA2244EL; RRID: AB_566585
Anti-mouse/human ERG (EPR3864)	Abcam	Cat# ab92513; RRID: AB_2630401
AF568 Donkey anti-Rabbit Secondary Antibody	Invitrogen	Cat# A10042; RRID: AB_2534017
AF488 Donkey anti-Rat Secondary Antibody	Invitrogen	Cat# A21208; RRID: AB_2535794
AF488 Donkey anti-Rat Secondary Antibody	Jackson Immuno Research	Cat# 712-545-153; RRID: AB_2340684
AF594 Donkey anti-Rat Secondary Antibody	Invitrogen	Cat# A21209; RRID: AB_2535795
AF594 Goat anti-Hamster Secondary Antibody	Jackson Immuno Research	Cat# 127-585-160; RRID: AB_2338999
AF488 Goat anti-Rabbit Secondary Antibody	Invitrogen	Cat# A11034; RRID: AB_2576217
AF568 Goat anti-Rabbit Secondary Antibody	Invitrogen	Cat# A11036; RRID: AB_10563566
AF647 Goat anti-Rabbit Secondary Antibody	Invitrogen	Cat# A21244; RRID: AB_2535812
AF488 Goat anti-Hamster Secondary Antibody	Invitrogen	Cat# A-21110; RRID: AB_2535759
AF594 Donkey anti-Goat Secondary Antibody	Jackson Immuno Research	Cat# 705-585-147; RRID: AB_2340433
AF488 Donkey anti-Rabbit Secondary Antibody	Invitrogen	Cat# A21206; RRID: AB_2535792

(*Continued on next page*)

Continued

REAGENT or RESOURCE	SOURCE	IDENTIFIER
AF647 Donkey anti-Rabbit Secondary Antibody	Invitrogen	Cat# A-31573; RRID: AB_2536183
AF647 Donkey anti-Rabbit Secondary Antibody	Jackson Immuno Research	Cat# 711-605-152; RRID: AB_2492288
AF488 Donkey anti-Goat Secondary Antibody	Jackson Immuno Research	Cat# 705-545-147; RRID: AB_2336933
ONCC9 (anti-CTLA4 nanobody)	Oncurious	N/A
P00200016 (LTbR agonist nanobody)	Oncurious	N/A
Biological samples		
Human breast cancer tissue: patient 12	This paper	N/A
Human breast cancer tissue: patient 16	This paper	N/A
Human breast cancer tissue: patient 20	This paper	N/A
Human breast cancer tissue: patient 21	This paper	N/A
Human breast cancer tissue: patient 23	This paper	N/A
Human breast cancer tissue: patient 24	This paper	N/A
Chemicals, peptides, and recombinant proteins		
Collagenase I	Worthington Biochemical	Cat# LS004214
Collagenase IV	Worthington Biochemical	Cat# LS004209
DNAse I	Worthington Biochemical	Cat# LS006333
Lymphoprep	stemcell technologies	Cat# 07851
Phorbol 12-myristate 13-acetate	R&D	Cat# 4153
Ionomycin calcium salt	R&D	Cat# 1704
Brefeldin A	R&D	Cat# 1231
Bovine serum albumin (BSA)	ThermoFisher	Cat# 10270–106
DMEM	ThermoFisher	Cat# 41965039
RPMI	Gibco	Cat# 21875–034
Fetal bovine serum (FBS)	SIgma	Cat# B4287
L-Glutamine	ThermoFisher	Cat# 25030024
Phosphate buffered saline (PBS)	ThermoFisher	Cat# 14190094
Triton-100	Sigma	Cat# T8787
Tween-20	Sigma-Merck	Cat# P9416
Tamoxifen	Sigma	Cat# T5648
10% Neutral buffered formalin	Sigma-Merck	Cat# HT501128
TopVision Low Melting Point Agarose	ThermoFisher	Cat# R0801
Lycopersicon Esculentum (Tomato) Lectin, DyLight® 488	ThermoFisher	Cat# L32470
7-AAD	eBioscience	Cat# 00-6993-50
Zombie Yellow™ Fixable Viability Kit	Biolegend	Cat# 423103
Fixable Viability Dye eFluor™ 780	eBioscience	Cat# 65-0865-14
Critical commercial assays		
CD45 (TIL) MicroBeads, mouse	Miltenyi	Cat # 130-110-618
CD326 (EpCAM) MicroBeads, mouse	Miltenyi	Cat# 130-105-958
Deposited data		
Raw and processed scRNA-seq Data	This paper	GEO: GSE198080
Human breast cancer Grand Challenge datasets	Bassez A et al.[31]	EGA: EGAS00001004809
Melanoma bulk RNA data (CA209-038)	Riaz N et al.[45]	GEO: GSE91061
NSCLC bulk RNA data (Poplar and PCD4989g)	Banchereau R et al.[47]	EGA: EGAS00001004343
Experimental models: Cell lines		
PyMT	Provided by Z.Werb	N/A
PyMT-OVA	Provided by M. Krummel	N/A
E0771	Provided by M. Mazzone	N/A
MC38	Kerafast	Cat# ENH204-FP

(*Continued on next page*)

Continued

REAGENT or RESOURCE	SOURCE	IDENTIFIER
Experimental models: Organisms/strains		
Mouse: FVB/NCrl	Charles River	Strain Code: 207
Mouse: C57BL/6NCrl	Charles River	Strain Code: 027
Mouse: Rag1 KO mice (FVB/N background)	Provided by D. Hanahan	N/A
Mouse: Confetti fl/+×Cdh5-CreER	Provided by S. Dimmeler	N/A
Mouse: Cdh5-CreER×LTβRlox/lox mice	This paper	N/A
Mouse: Chst4-Cre(ER)T2/iRFP mice	This paper	N/A
Mouse: Chst4-tdT reporter mice	This paper	N/A
Oligonucleotides		
Oligonucleotides: see Table S1	This paper	N/A
Primers: see Table S1	This paper	N/A
Software and algorithms		
R version 4.1.0 (2021-05-18) Platform: ×86_64-w64-mingw32/×64 (64-bit) Running under: Windows 10 × 64 (build 19041)	R Core Team	https://www.r-project.org
Seurat_4.0.3	CRAN	https://CRAN.R-project.org/package=Seurat
SeuratObject_4.0.2	CRAN	https://CRAN.R-project.org/package=SeuratObject
ggplot2_3.3.5	CRAN	https://CRAN.R-project.org/package=ggplot2
ggpubr_0.4.0	CRAN	https://CRAN.R-project.org/package=ggpubr
harmony_0.1.0	CRAN	https://CRAN.R-project.org/package=harmony
AUCell_1.14.0	Bioconductor	https://bioconductor.org/packages/AUCell
GSVA_1.40.1	Bioconductor	https://bioconductor.org/packages/GSVA
SeuratExtend_0.5.1	This paper	https://github.com/huayc09/SeuratExtend
SCENIC Nextflow pipeline	Aibar S et al.[28]	https://github.com/aertslab/scenic-nf
Python_3.8.3	Python	http://www.python.org/
Palantir_0.2.6	Setty M et al.[32]	https://github.com/dpeerlab/Palantir
Scvelo_0.2.2	Bergen V et al.[33]	https://scvelo.readthedocs.io/
Velocyto_0.17.17	La Manno G et al.[34]	http://velocyto.org/
Cell Ranger	10x Genomics	N/A
CytoScape_3.8.2	Shannon P et al.[66]	http://cytoscape.org/
QuPath_0.3.0	Bankhead P et al.[68]	https://qupath.github.io/
Fiji/ImageJ, 1.53c	NIH	https://fiji.sc/
GraphPad Prism 9.2	Dotmatics	https://www.graphpad.com/
FlowJo version 10.8.0	BD	https://www.flowjo.com/
Cytobank	Beckman Coulter	https://premium.cytobank.org/cytobank
Codes of visualizing scRNA-seq data	This paper	https://doi.org/10.5281/zenodo.7255861

RESOURCE AVAILABILITY

Lead contact

Further information and requests for resources and reagents should be directed to and will be fulfilled by the lead contact, Gabriele Bergers (Gabriele.bergers@kuleuven.be).

Materials availability

Reagents generated in this study will be made available on request, but we may require a payment and/or a completed Materials Transfer Agreement if there is potential for commercial application.

Data and code availability

- For scRNA-seq data, all murine raw and processed sequencing data (Smartseq2 TU-HEV, TU-EC, and LN-HEV, 10X PyMT/E0771 UT/DPAg EC and IC, PyMT DPAg + anti-IFNg EC) are available in GEO under the accession number GSE198080 and will be publicly available as of the date of publication. Accession and identification numbers are listed in the key resources table.

To ensure data accessibility to non-bioinformaticians, we made the murine EC scRNA-seq data available for further exploration via an interactive web tool generated by ShinyCell[58] at https://bergers-lab.shinyapps.io/scrna_hev_smartseq2/and https://bergers-lab.shinyapps.io/scrna_mouse_bc_ec_10x/. With this tool, users can interactively visualize gene expression and clustering on tSNE/UMAP, or by violin plots, heatmap, or dot plots. The human breast cancer EC datasets are accessible from the European Genome-phenome Archive (EGA) under study no. EGAS00001004809.[31] For bulk RNA-seq immunotherapy datasets, melanoma cohort (CA209-038 study)[45] datasets are accessible from the GEO database with the accession number GSE91061. NSCLC datasets (Poplar and PCD4989g study) are accessible from EGA with the accession number EGAS00001004343.[46–48] All other data reported in this paper will be shared by the lead contact upon request.

- The original code for visualizing scRNA-seq data has been deposited at Zenodo and is publicly available. DOI is listed in the key resources table.
- Any additional information required to reanalyze the data reported in this paper is available from the lead contact upon request.

EXPERIMENTAL MODEL AND SUBJECT DETAILS

Cell lines

The luminal breast cancer PyMT cell line was generated from FVB/N MMTV-PyMT mammary tumor and was a kind gift from Dr. Zena Werb, University of California San Francisco. The PyMT-OVA cell line in the C57BL/6 background was provided by Dr. Max Krummel, University of California San Francisco.

The E0771 clone MC3B with metastatic potential to the lung (referred to as E0771) was kindly provided by Dr. Massimiliano Mazzone, VIB-KU Leuven, Belgium. The colon adenocarcinoma MC38 cell line was obtained from Kerafast. PyMT, PyMT-OVA, and MC38 cells were cultured with DMEM (Gibco) supplemented with 10% Fetal Bovine Serum (ThermoFisher), 1% glutamine, 100U/mL penicillin, and 100U/mL streptomycin. E0771 were cultured with RPMI (Gibco) supplemented with 10% Fetal Bovine Serum (Gibco), 1% glutamine, 100 U/mL penicillin, and 100 U/mL streptomycin. All cell lines were tested for mycoplasma every 3–5 passages.

Animal strains

Animal procedures were approved by the Institutional Animal Care and Research Advisory Committee of the KU Leuven (ECD 170/2016) and were performed following the institutional and national guidelines and regulations. C57BL/6, FVB/N mice were purchased from Charles River or obtained from the KU Leuven animal facility. Rag1 KO mice in an FVB/N background were in-house bred.

Conditional LTβR *knockout* mice (Cdh5-Cre^{ER}×LTβR$^{lox/lox}$ mice) were generated in a C57BL/6J background by intercrossing LTβR$^{lox/lox}$ mice with the tamoxifen-inducible, endothelial cell-specific Cdh5-CreER mouse line. Cdh5-CreER^{neg}×LTβR$^{lox/lox}$ mice littermates were used as controls.

Confetti$^{fl/+}$×Cdh5-Cre^{ER} mice in the C57BL/6J background[35] were kindly provided by Dr. Stefanie Dimmeler from the Goethe University Frankfurt, Germany.

Chst4-Cre(ER)T2/iRFP mice were generated by ES-cell injection into fertilized blastocysts to generate chimeric mice, which were consequently bred with C57BL/6 albino animals to generate homologous recombinant mice. ES cells harbored recombination of the following constructed transgene: The 5′ homology arm was comprised of 5836 bp of the Carbohydrate Sulfotransferase 4 (Chst4) promoter and 5′UTR, followed by the sequence encoding the first six amino acids (AA) of the CHST4 protein fused to AA 2–309 of iRFP670, a near-infrared fluorescent protein that does not overlap with EGFP and tdTomato. An internal ribosomal entry site (IRES) preceded Cre-ERT, an SV40 poly-A signal, and a loxP site. An SV40 promoter drove the expression of a neomycin resistance gene, followed by an SV40 poly-A signal, another loxP site, and a 3613 bp 3' Chst4 homology arm with a third loxP site.

Chst4-tdT reporter mice (C57BL/6J) were generated by intercrossing the tamoxifen-inducible Chst4-Cre(ER)T2/iRFP mice with Rosa26-LSL-tdTomato reporter mice.

Conditional LTβR deletion (Cdh5-Cre^{ER}×LTβR$^{lox/lox}$ mice), the stochastic multicolor recombination in the endothelial cells (Confetti$^{fl/+}$×Cdh5-Cre^{ER} mice), and the tdTomato labeling of TU-HEVs were achieved by intraperitoneal injections of Tamoxifen (Sigma-Aldrich) (2 mg/mouse/day) for five consecutive days prior to orthotopic implantation of PyMT-OVA or subcutaneously injected MC38 cancer cells.

For all experiments, animals were maintained in individually ventilated cages in a room with controlled temperature and humidity under a 12-h light/12-h dark cycle with *ad libitum* access to water and food. Information on age and sex of mice can be found in the 'method details'-section.

Human samples

The collection of breast cancers used for the MILAN staining was conducted under the license ETMK: 132/2016. Written informed consent for donating tissue was obtained from each patient. The samples were kept anonymously and handled according to the ethical guidelines set by the University of Turku. All patients were treatment-naive and had lymph node metastasis.

Patient 12: Ductal luminal, ER+; Female, age 54
Patient 16: Lobular luminal, ER+; Female, age 50.
Patient 20: Ductal luminal, ER+; Female, age 65.

Patient 21: Ductal, Her 2+; Female, age 44.
Patient 23: Triple-negative; Female, age 47.
Patient 24: Ductal luminal, ER+; Female, age 68.

METHOD DETAILS

Mouse trials

6 to 8-week-old FvB/N or C57BL/6 female mice were anesthetized, and a small incision in the skin of the lower abdomen was made to allow the orthotopic injection of 1×10^6 PyMT or 2.5×10^5 E0771 into each 4th mammary fat pad. 1×10^6 MMTV-PyMT-OVA were orthotopically injected in 9 to 14-week-old Chst4-tdT reporter mice, 8 to 11-week-old Cdh5-Cre^{ER}×LTβR$^{lox/lox}$ mice, and 27-week-old Confetti$^{fl/+}$×Cdh5-Cre^{ER} mice.

5×10^5 MC38 cells were subcutaneously injected into the flank of 6 to 8-week-old C57BL/6 female mice.

Treatment started when the tumors reached a volume of 100–150 mm^3. Mice were treated with 20 or 40 mg/kg DC101 (BioXcell), 10 mg/kg anti-PD-L1 (BioXcell), 2 mg/kg LTβR agonist (Biorad), 2 mg/kg LTβR agonist (Oncurious), 5 mg/kg anti-CTLA-4 (CD152) (BioXcell), 1 mg/kg anti-CTLA-4 (Oncurious), or 10 mg/kg IgG2b isotype control. All drugs were injected intraperitoneally (i.p.).

PyMT- bearing mice received the DC101 + anti-PD-L1 + LTβR Agonist (DPAg) treatment twice a week for 10–13 days.

E0771-bearing mice received the 40 mg/kg DC101 + anti-PD-L1 + LTβR Agonist (DPAg) treatment twice a week for 8 days (Figure 4), or IgG/20 mg/kg DC101/LTβR Agonist (Oncurious)/DC101 + LTβR Agonist (Oncurious) twice a week for 14 days (Figure S6).

MC38-bearing mice were treated biweekly for 2 to 3 weeks with 2 mg/kg LTβR Agonist (Oncurious) and weekly with 1 mg/kg anti-CTLA-4 (Oncurious), or biweekly with 20 mg/kg DC101 and 2 mg/kg LTβR Agonist (Oncurious) starting seven days after cancer cell implantation.

8 to 11-week-old Cdh5-Cre^{ER}×LTβR$^{lox/lox}$ female or male mice were used in this study. PyMT-OVA-bearing mice received the DC101 + anti-PD-L1 + anti-CTLA-4 (BioXcell) (DPC) therapy every second day for 7 to 10 days. MC38-bearing mice were treated with the DC101 + anti-PD-L1 + anti-CTLA-4 (Oncurious) biweekly for 20 days, or anti-CTLA4 (Oncurious) + LTbR Ag (Oncurious) biweekly for 14 days.

9 to 14-week-old female or male Chst4-tdT reporter mice were used in this study. PyMT-OVA-bearing mice were treated with DC101 + anti-CTLA-4 (Oncurious) + LTβR Agonist (Biorad) every second day for nine days, and subcutaneous MC38-bearing mice were treated with anti-CTLA4 (Oncurious) + LTβR Ag (Oncurious) biweekly for 11 days. Tamoxifen was injected six days after treatment initiation (2 mg/d, until sac the on-treatment mice).

27-week-old female PyMT-OVA-bearing Confetti$^{fl/+}$×Cdh5-Cre^{ER} mice were treated with DPAg every second day for nine days.

IFNγ was blocked by biweekly administration of 200 mg/mouse of anti-mouse IFNγ (clone XMG1.2) (BioXCell) starting one day before the DPAg treatment until the end of the trial. For the immune cell depletion experiments, mice were injected i.p. with 0.5 mg anti-CD8 (clone 2.43), or anti-CD4 (clone GK1.5), or anti-NK1.1 (clone PK136), or anti-CSF1R (clone AFS98), or IgG2b (clone LTF-2) for three consecutive days before the start of DPAg treatment followed by weekly injection of 1mg of anti-CD8 or anti-CD4 or 0.5 mg of anti-NK1.1 or 0.5 mg of anti-CSF1R every second day until the end of the trial. All the depleting antibodies are purchased from BioXCell. Blood was collected before and after DPAg treatment to validate depletion efficiency by flow cytometry.

The t_0 time point in the tumor growth curves indicates the treatment start. Unless differently specified, mice were sacrificed the day after the last treatment.

The tumor size was measured twice a week, and the tumor volume was calculated using the following formula to approximate the volume of an ellipsoid: $(\text{width})^2$ x length x 0.52.

Tissue dissociation and sample preparation

For immune cell analysis, tumors were excised, mechanically minced, and incubated with serum-free RPMI containing 3 U/mL Collagenase I (Worthington Biochemical), 133 U/mL Collagenase IV (Worthington Biochemical), and 10 U/mL DNAse I (Worthington Biochemical) and rotated at 37°C for 30 min. Enzymatic digestion was blocked by adding RPMI-1640 containing 2mM EDTA and 2% FBS. The remaining tumor aggregates were dissociated mechanically. The single cell suspension was then passed through a 70μm strainer and red blood cells were lysed by incubation with 3 mL of ACK Lysis Buffer (15 mM NH_4Cl, 10 mM $KHCO_3$, 0.1 mM Na_2EDTA) for 3 min at RT. For the immune characterization of PyMT and E0771 tumors upon DPAg treatment and at treatment cessation, and for the isolation of immune cells for the scRNA-seq analysis, tumor-infiltrating lymphocytes were further enriched using Lymphoprep (Stemcell technologies) and density gradient centrifugation (800 × g for 30 min, without break or acceleration, RT). The interphase cells were collected and washed with PBS before flow cytometry staining.

For TU-HEV analyses, tumors were minced and incubated with enzymes A, D, and R (Tumor Dissociation Kit, Miltenyi) in combination with mechanical dissociation by gentleMACS™ Dissociator (Miltenyi). Tumor endothelial cells were enriched by removing immune cells and tumor cells using the positive selection anti-mouse CD45 (TIL) MicroBeads (Miltenyi) and the positive selection anti-mouse CD326 (EpCAM) MicroBeads (Miltenyi). The negative fraction that contained the remaining endothelial cells was collected and washed with PBS before flow cytometry staining.

Flow cytometry

Single cell suspensions were blocked using 2.4G2 hybridoma supernatant or anti-CD16/32 blocking antibody (BD Biosciences). Samples were stained for 30 min on ice with antibody cocktails covering: CD31 (clone 390), MECA-79 (clone MECA-79), LTβR (clone 5G11), CD3 (clone 17A2), CD4 (clone GK1.5; clone RM4-5), CD8α (clone 53–6.7), 70), CD11c/70), CD11c (clone N418), CD19 (clone 1D3;B4), CD45 (clone 30-F11), CD62L (clone MEL-14), CD44 (IM7), CD64 (clone X54-5/7.1), CD172a (clone P84), Foxp3 (clone REA788), Granzyme B (clone NGZB; clone QA16A02), IFN-γ (clone XMG1.2), Ly6C (clone HK1.4), Ly6G (clone 1A8), MHC-II (clone M5/114.15.2), NK1.1 (clone PK136), PD-1 (clone 29F.1A12), PDCA-1 (clone REA818), TCR-β (clone H57-597), TNF-α (clone MP6-XT22), XCR1 (clone ZET), TCF-1 (clone C63D9), Ki67 (clone 16A8), NKp46 (clone 29A1.4), T-bet (clone 4B10), CD25 (clone PC61), CD127 (clone SB/199), and TIM-3 (clone RMT3-23) from Cell Signaling, Biolegend, BD Bioscience, eBioscience and Miltenyi Biotec. Dead cells were excluded using the Fixable Viability Dyes (eBioscience, Biolegend) or 7AAD (eBioscience).

For intracellular cytokine staining, lymphocytes were plated in U-bottom 96-well tissue-culture plates in complete RPMI containing phorbol 12-myristate 13-acetate (500 ng/mL Bio-Techne), ionomycin (750 ng/mL, Bio-Techne), and brefeldin A (2 μg/mL; Bio-Techne) for 4 h at 37°C. Cells were blocked with 2.4G2 hybridoma supernatant in combination with mouse IgG (ThermoFisher) for 20 min at 4°C. Cells were fixed with 2% formalin and permeabilized by Foxp3/Transcription Factor Staining Buffer Set (ThermoFisher) before intracellular staining. For transcriptional factor staining, single-cell suspension was fixed and permeabilized by Foxp3/Transcription Factor Staining Buffer Set (ThermoFisher) before intracellular staining.

TIL data were acquired on a BD FACSymphony or BD FACSCanto II (BD Biosciences). Conventional CD4 T cells and Treg cells were sorted by a BD FACS Aria Fusion (BD Biosciences).

Endothelial cell-related data were acquired on a BD FACSCanto II, $CD31^+$ $MECA79^-$ ECs, and $CD31^+MECA79^+$ HEV cells were sorted with a BD FACSAria III (BD Biosciences). Results were analyzed with FlowJo version 10.8.0 (Becton Dickinson, Ashland) and the Cytobank software (https://premium.cytobank.org/cytobank).

In S4E, fcs files were analyzed using the Cytobank software. Samples were pre-gated for single live $CD45^+$ cells and tSNE plots showing 500.000 cells were generated using 1500 iterations, a perplexity of 45, and a theta value of 0.3.

Gene expression analysis

RNA was extracted from tumor lysates using the TRIzol™ reagent (Life Technologies) and the PureLink™ RNA Mini Kit (Thermo Fisher Scientific) according to the manufacturer's instructions. Pre-amplified cDNA from tumor lysates was made using the SuperScript™ III First Strand cDNA Synthesis Kit (Thermo Fisher Scientific) according to the manufacturer's protocol. qPCR was then performed on a CFX96™ Real-Time System instrument (Biorad) by using the pre-amplified cDNA for the target genes. qPCR analysis was performed using Power-Up SYBR green mastermix (Thermo Fisher Scientific). Relative gene expression was calculated as previously described.[18] In brief, *Rpl19* was used as housekeeping genes to generate ΔCt. ΔCt values from untreated mice were used as a reference for the treatment groups to generate ΔΔCt, and relative gene expression was calculated as 2(-ΔΔCt). All reactions were run in duplicate. Primers are listed in Table S1.

Immunostaining

For the preparation of frozen sections, excised tumors and lymph nodes were fixed in 2% paraformaldehyde (PFA) at 4°C overnight, followed by 30% sucrose at 4°C overnight before being embedded in OCT (Leica). For the preparation of agarose sections, tissues were fixed in 2% PFA at 4°C for 24h, then embedded in 4% low melting agarose (in PBS).

For analysis of lectin perfusion, Lycopersicon esculentum agglutinin (LEA, tomato lectin; Invitrogen) was intravenously injected (50μg/100μL). 15'after injection, mice were deeply anesthetized and perfused with PBS and then 2% PFA through the heart before tissue collection.

8μm thick or 100μm thick tumor tissue sections were stained with anti-MECA79 (clone MECA-79), anti-TCF1 (clone C63D), anti-CD8a (53–6.7), anti-PD-1 (polyclonal), anti-CD3 (17A2), anti-B220 (RA3-6B2), anti-CD4 (RM4-5), anti-FOXP3 (FJK-16s), anti-CD31 (polyclonal; 2H8), anti-TIM3 (E9K5D), anti-desmin (polyclonal). When primary antibodies were unlabeled, fluorophore-conjugated secondary antibodies were used. Images were taken with an Observer Z1 microscope (Zeiss) linked to an AxioCam MRM camera (Zeiss) with objectives of 20X magnification or Leica Confocal SP8 with objectives of 20X or 63X magnification.

HEV quantification on tissue sections was assessed by quantifying the number of $CD31^+$ $MECA79^+$ tumor vessels. When specified, the HEV number was normalized to the non-necrotic tumor area. For evaluation of necrotic areas, frozen tumor sections were stained with hematoxylin-eosin (H&E). H&E sections were subsequently imaged under fluorescence conditions (577nm excitation wavelength) using an Observer Z1 microscope (Zeiss) (10× magnification) or Zeiss AxioScan.Z1 (20× magnification), allowing for identification of necrotic regions through autofluorescent properties of necrotic cells.[18] The non-necrotic area was measured by subtracting the necrotic area from the total tumor area.

Image analysis and quantitation were performed using ImageJ software version 2.0.0.

MILAN multiplex immunohistochemistry

Tissue staining

Multiple Interactive Labeling by Antibody Neodeposition (MILAN) immunohistochemistry was performed according to a previously published method.[44,59,60] Tissue sections (3–5 μm) were prepared from FFPE murine MC38 samples and human breast cancer samples. Following dewaxing, antigen retrieval was performed using PT link (Agilent) using 10 mM EDTA in Tris-buffer pH 8.

Immunofluorescence staining was performed using Bond RX Fully Automated Research Stainer (Leica Biosystems) with the following primary antibodies: anti-CD31 (polyclonal; clone OTI2C6); TIM3 (clone EPR22241; polyclonal); CD8 (clone 4SM15; clone C8/144B); PD1 (clone D7D5W, clone D4W2J), GrzB (polyclonal); Ki67 (clone D3B5; clone UMAB107); MECA79 (clone MECA79); TCF1 (clone C63D9); perforin (clone 5B10). The sections were incubated for 4 h with the primary antibodies, washed, and then incubated for 30 min with secondary antibodies. To amplify the signal, negative-isotype controls were added for 30 min, followed by a second incubation with the same secondary antibody for 30 min after three washing steps. A coverslip was placed into the slides with a medium containing 4,6-diamidino-2-phenylindole (DAPI) and scanned using a Zeiss AxioScan Z.1 (Zeiss) at 10X magnification. The coverslips were removed after 30 min soaking in washing buffer. Stripping of the antibodies was performed in a buffer containing 1% SDS and β-mercaptoethanol for 30 min at 56°C. After. The staining procedure was repeated for several rounds until all markers were stained and scanned.

Image processing

Sequential rounds were aligned using an FFT-based registration method[61] in the DAPI channel of every round. Cell objects were defined using Stardist[62] in the DAPI channel for the first round. Signal autofluorescence was removed by applying a weighted subtraction of the reference round. A mask for every marker (CD8, CD31, MECA79, PD1, TIM3, TCF1, Ki67, GrzB) was obtained by applying a high-pass filter with an adaptive threshold. $CD8^+$ objects were identified as the segmented cells with 50% or more overlap with the CD8 mask. The following structures of interest were defined using these masks: $TCF1^+$ $PD1^+$ $TIM3^-$ = $CD8^+$ pT_{EX}; $TCF1^-PD1^+TIM3^+$ = $CD8^+$ tT_{EX}; $TCF1^+PD1^-TIM3^-$ = $CD8^+$ TCF1 cells; $CD31^+MECA79^-$ = blood vessels; $CD31^+MECA79^+$ = HEVs. The rest of the CD8 T cells were identified as "not otherwise specified" (NOS).

Data analysis

By segmenting the tissue in areas of 100 sq micrometers, we then classified the tissue into different vascular areas dependent on the percentage of $MECA79^+CD31^+$ HEVs and $MECA79^{neg}$ $CD31^+$ BVs. If more than 25% of the vessels inside each area were HEVs, the area was considered HEV-high, if less, HEV-low. If $CD31^+$ BVs were sparsely apparent or non-apparent, the area was considered non-vascular. Two expert pathologists (Dr. Francesca Maria Bosisio and Dr. Giuseppe Floris) independently annotated the tissue sections in three different areas: tumor-bulk, tumor-edge, and non-tumor. The percentage of the defined CD8 T cell subsets (pT_{EX} vs pT_{EX} vs $TCF1^+PD1^-$ vs NOS), as well as their proliferation status ($Ki67^+$) and cytotoxicity (average levels of GrzB and perforin), was measured in the different tumoral and vascular areas. The statistical test used was the Wilcoxon signed-rank test, with the adjusted p-value using Holm correction. Adjustment for multiple tests was performed using the false-discovery-rate (FDR) method.

Single-cell RNA sequencing

10X Genomics

The single cell suspensions were converted to barcoded scRNA-seq libraries using the Chromium Single Cell 3′ Library, Gel Bead & Multiplex Kit, and Chip Kit (10x Genomics), aiming for 6,000 cells per library. Samples were processed using kits pertaining to V2 barcoding chemistry of 10x Genomics. Single samples were always processed in a single well of a PCR plate, allowing all cells from a sample to be treated with the same master mix and in the same reaction vessel. For each experiment, all samples were processed in parallel in the same thermal cycler. Libraries were sequenced on an Illumina HiSeq4000, and mapped to the human genome (buildGRCh38) or to the mouse genome (build mm10) using CellRanger software (10x Genomics, version 3.0.2).

SmartSeq2

$CD45^-CD31^+MECA79^+$ cells (TU-HEV and LN-HEV) or $CD45^-CD31^+MECA79^-$ (TU-EC) cells were sorted (BD FACSAria III) in 96 well plates (VWR, DNase, RNase free) containing 2 μL of lysis buffer (0.2% Triton X-100, 4U of RNase inhibitor, Takara) per well. Plates were properly sealed and spun down at 2000 g for 1 min before storing at −80°C. Whole transcriptome amplification was performed with a modified SMART-seq2 protocol as described previously,[63] using 23 instead of 18 cycles of cDNA amplification. PCR purification was realized with a 0.8:1 ratio (ampureXP beads:DNA). Amplified cDNA quality was monitored with a high sensitivity DNA chip (Agilent) using the Bioanalyzer (Agilent). Sequencing libraries were performed using the Nextera XT kit (Illumina) as described previously,[63] using 1/4th of the recommended reagent volumes and 1/5th of input DNA with a tagmentation time of 9 min. Library quality was monitored with a high-sensitivity DNA chip (Agilent) using the Bioanalyzer (Agilent). Indexing was performed with the Nextera XT index Kit V2 (A-D). Up to 4 × 96 single cells were pooled per sequencing lane. Samples were sequenced on the Illumina NextSeq 500 platform using 75bp single-end reads.

Single-cell transcriptomics analysis

Quality control, data cleaning, and normalization

Raw gene expression matrices generated per sample were analyzed with the Seurat3 package in R.[64] For Smart-Seq2 datasets (Figure 1), three samples (TU ECs, TU HEVs and LN HEVs) were merged together, and cells were filtered by nFeature_RNA (genes detected) > 2000 and percent.mt (percentage of mitochondria genes) < 20. For mouse 10X datasets (Figure 2), 5 samples (E0771 UT, E0771 DPAg, PyMT UT, PyMT DPAg, PyMT DPAg + anti-IFNγ) were merged together and cells were filtered by nCount_RNA (unique molecular identifiers, UMIs) > 5000 and percent.mt < 10. For human 10X datasets (Figure 2), 55 samples (from 28 patients) from the VIB Grand Challenges Program (GCP) were merged, and cells were filtered by nFeature_RNA >1000 and percent.mt < 15. After filtering cells, log-normalization was performed using the default NormalizeData function in Seurat. For 10X datasets (mouse and human), in silico EC selection was done by using the basic Seurat pipeline of cell clustering with default parameters, followed by EC-related cluster annotation based on canonical markers, including Pecam1/PECAM1 and Cdh5/CDH5 (ECs), Prox1/PROX1

(lymphatic ECs) and Pdgfrb/PDGFRB (pericytes) to discriminate ECs from contaminating cells. The following analyses were done on ECs only.

Dimension reduction, sample integration, clustering, and visualization

High variable genes were selected by FindVariableFeatures and auto-scaled by ScaleData function, and a principal component analysis (PCA) was performed for all datasets using the default RunPCA function in the Seurat package. For the Smart-Seq2 datasets (Figure 1), t-distributed stochastic neighbor embedding (tSNE)[65] was performed using the RunTSNE function in Seurat, using PCA dimensions 1 to 5, and clustering based on the sample origin (TU EC, TU HEV, and LN HEV). For the mouse 10X Genomics datasets (Figure 2), batch effect correction of each sample was done using the Harmony algorithm (Korsunsky et al., 2019) based on PCA space, followed by uniform manifold approximation and projection (UMAP) using RunUMAP step (dims = 10) for data visualization, and FindNeighbors followed by FindClusters function (dims = 10, resolution = 0.55) in the Seurat package for unsupervised clustering. For the human breast cancer datasets[31] (Figure 3), batch effect correction of each sample was done using the Harmony algorithm, followed by UMAP (dims = 5) for data visualization, and unsupervised clustering (dims = 6, resolution = 0.55) in Seurat. The EC subtypes were identified mainly based on marker genes reported in the literature.[29]

SCENIC and gene set enrichment analysis

To carry out the transcription factor network inference, SCENIC workflow was performed using Nextflow pipeline,[28] and regulon activity of each cell was evaluated using AUCell score with Bioconductor package AUCell. Graphs with modes and edges (Figures 1G and S1E) were generated by CytoScape.[66] For functional/pathway analysis, gene set lists were collected from databases including Gene Ontology (GO), Reactome, and Hallmark geneset of MSigDB database (http://www.gsea-msigdb.org/). For Gene Set Enrichment Analysis (GSEA), the enrichment of given gene sets of each cell was evaluated using AUCell package as well.

Trajectory analysis

For mouse 10X datasets, we first integrated the datasets by tumor model and anti-IFNγ treatment using Harmony algorithm, and used Python package Palantir[32] to calculate diffusion map based on Harmony space, then diffusion components and visualized the data by tSNE. To predict the differentiation direction, we conducted a Velocyto pipeline[34] using the *.bam file and barcode information generated by CellRanger, and used ScVelo in Python[33] for better visualization. The differential potential of each cell was predicted using either CytoTRACE[67] or the Palantir algorithm.

Differential expression analysis and data visualization

Differentially expressed genes (DEGs) were identified by the Wilcoxon Rank Sum test using the FindMarkers function in Seurat. Gene expression levels or gene set enrichment scores (AUCell score) were shown in t-score or z-score for heatmaps or waterfall plots. UMAP or tSNE plots were done using DimPlot or FeaturePlot functions in Seurat. Heatmaps, modified stacked violin plots, waterfall plots, bar plots of cluster proportion, and GSEA plots were generated using customized codes in R, and these functions were integrated into the R package ''SeuratExtend'' which is available on Github (https://github.com/huayc09/SeuratExtend).

Bulk RNA sequencing analysis

Selection of human tumor HEV signatures

Candidate human tumor HEV genes were identified by selection from: 1) conserved mouse and human tumor HEV genes for RNAscope experiment (C1S, CHST4, CSF2RB, FUT7, IL2RG, LIPG) (Figures 2M–2O); 2) other conserved tumor HEV genes (ENPP2, KIT, LIFR, SERPINB9) (Figures S3F and S3G) and 3) Top human lymph node HEV marker genes from publicly available head and neck cancer single cell datasets (SLAMF1, CH25H, TMEM176A, C4BPA, ENPP6) (Puram et al., 2017). Next, genes were removed that are more enriched in other cell types than EC (C1S highly expressed in CAF; TMEM176A in Mac/CAF; IL2RG, SLAMF1, SERPINB9 in T/B cells; CSF2RB in pDC; KIT in mast cell). The remaining eight HEV genes were used for further GSEA analysis (CHST4, FUT7, LIPG, ENPP2, LIFR, CH25H, C4BPA, ENPP6).

GSEA and statistical analysis

Enrichment scores of the human tumor HEV signature were calculated using gsva method by GSVA package in R, and ggpubr package was used for data visualization and statistical analysis using default Wilcox test.

RNAscope in situ *hybridization and quantification*

For the preparation of Formalin-Fixed Paraffin Embedded (FFPE) sections, tumors were excised and fixed in 10% neutral buffered formalin (Sigma-Merck) for 20 h at +4°C, dehydrated, and embedded in paraffin. 5μm thick FFPE sections were subjected to RNAscope *in situ*, hybridization using the RNAscope Multiplex Fluorescent v2 assay (ACDBio) according to the manufacturer's instructions (USM-323100 Multiplex Fluorescent v2 User Manual, MK-5150_TN Multiplex Fluorescent V2 with ICW and 4-Plex Ancillary Kit for Manual multiplex fluorescent kit). Briefly, after deparaffinization, the slides were incubated with hydrogen peroxide for 10 min at RT. After washing, manual target retrieval was performed, followed by incubation with primary antibody at 4°C ON. Protease Plus was,d followed by hybridization with the RNAscope probes and the RNAscope 3-plex Positive (low expression Polr2a, medium expression PPIB, and high expression UBC) and Negative Control Probes. A negative control probe targeting a bacterial gene was used to assess the background. Slides were then processed according to the RNAscope Multiplex Fluorescent v2 protocol (Hybridization, Amplification, and Signal Development) before secondary antibody incubation. RNAscope probes are listed in key resources table and Table S1. Images were acquired using Vectra® Polaris™ Automated Quantitative Pathology Imaging System. For quantification, the QuPath software was used to auto-detect cells and subcellular particles following the tutorial on ACDBio website (2021 Mar 30 - ACD Support Webinar: Visualization and Analysis of RNAscope™ Results using QuPath).

QUANTIFICATION AND STATISTICAL ANALYSIS

Data entry and all analyses were performed in a blinded fashion. In Figure 5B, the tumor size measurement has been taken at the indicated timepoints +/− one day. In Figures 4B and S4C and S4I, the label 8D off is referred at samples collected 8–9 days after treatment cessation; the label 18D off is referred at samples collected 14–20 days after treatment cessation.

Bar graphs show mean values ± SEM. Unpaired Student's t-test (two-tailed) (Mann-Withney U test) was used for the comparison of the two groups. The Wilcoxon test was used to compare two paired groups. Kruskal-Wallis test or 2way ANOVA was used for comparing >2 groups as indicated in the corresponding legends. Statistics were indicated only when significant.

Boxplots in this manuscript were made by ggplot2 package in R. It visualizes five summary statistics (the median, two hinges and two whiskers). The lower and upper hinges correspond to the first and third quartiles (the 25th and 75th percentiles). The upper whisker extends from the hinge to the largest value no further than 1.5 * IQR from the hinge (where IQR is the inter-quartile range, or distance between the first and third quartiles). The lower whisker extends from the hinge to the smallest value at most 1.5 * IQR of the hinge.

p values <0.05 were considered significant (*: $p < 0.05$; **: $p < 0.01$; ***: $p < 0.001$; ****: $p < 0.0001$). All statistical analyses were performed using GraphPad Prism software (Version 9.2) or ggpubr package in R.

Cancer Cell, Volume *40*

Supplemental information

Cancer immunotherapies transition endothelial cells into HEVs that generate TCF1^{+} T lymphocyte niches through a feed-forward loop

Yichao Hua, Gerlanda Vella, Florian Rambow, Elizabeth Allen, Asier Antoranz Martinez, Marie Duhamel, Akira Takeda, Sirpa Jalkanen, Steffie Junius, Ann Smeets, David Nittner, Stefanie Dimmeler, Thomas Hehlgans, Adrian Liston, Francesca Maria Bosisio, Giuseppe Floris, Damya Laoui, Maija Hollmén, Diether Lambrechts, Pascal Merchiers, Jean-Christophe Marine, Susan Schlenner, and Gabriele Bergers

Supplemental figure 1

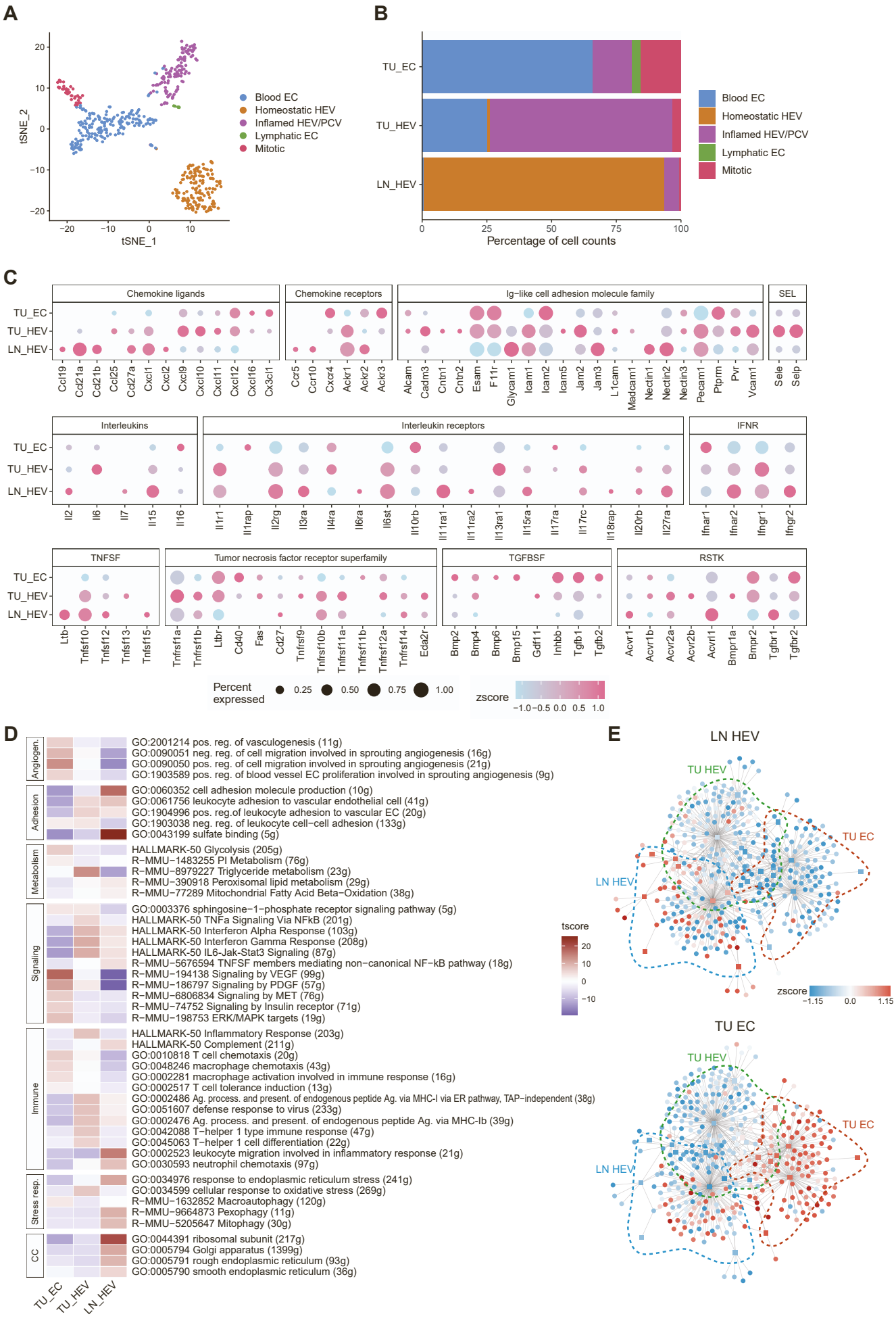

Figure S1. General characterization of TU-HEVs, LN-HEVs and TU-ECs, related to Figure 1

(A) tSNE plot of EC transcriptomes, colored by cell type.

(B) Fraction of EC sub-groups in TU-HEV, LN-HEV and TU-EC.

(C) Expression of selected chemokines, adhesion molecules and cytokines (ligand + receptor, x axis) in three EC samples (y-axis). Dot size represents the percentage of cells in which the gene is detected. Color indicates the mean expression (in z-score).

(D) Heatmap showing selected pathway activities in TU-EC, TU-HEV and LN-HEV.

(E) Gene regulatory network (GRN) predicted by SCENIC. Node color shows the gene expression (round nodes) and regulon activity (square node) in LN-HEV and TU-EC.

Data are from one scRNA-seq experiment.

Supplemental figure 2

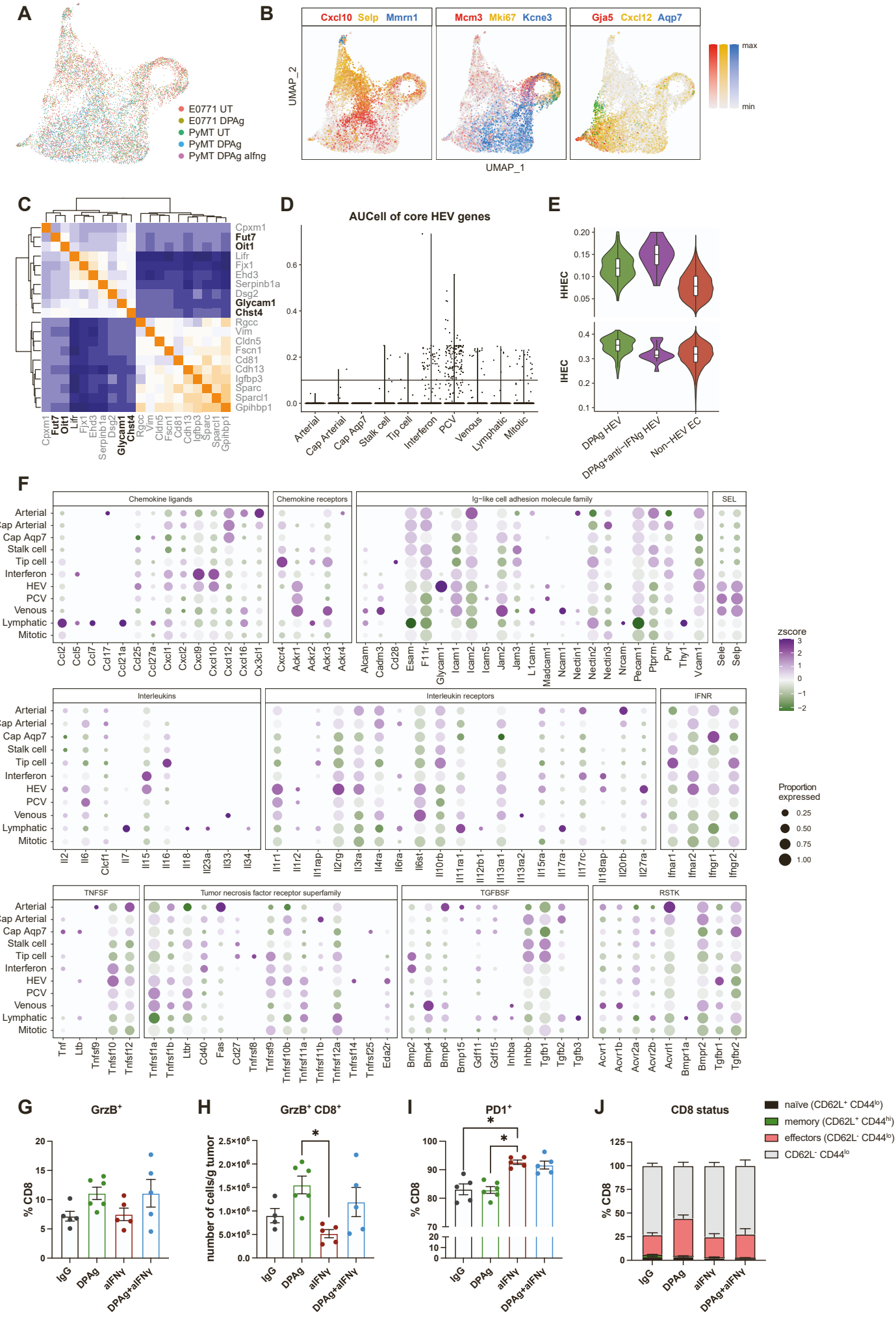

Figure S2. Characterization of the mouse tumor vasculature by droplet-based scRNAseq, related to Figure 2

(A) UMAP plot, colored by samples integrated by Harmony algorithm.

(B) Expression level of representative marker genes to annotate EC subtypes.

(C) Pearson correlation matrix heatmap showing the top 10 positive and negative correlated genes with Chst4.

(D) AUCell of core HEV genes in each cell. AUCell > 0.1 are defined as HEVs.

(E) Violin plots showing the AUCell of gene signatures of HHEC (homeostatic HEC) and IHEC (inflammatory HEC) in DPAg HEVs, DPAg + anti-IFNγ HEVs and other ECs.

(F) Expression of selected chemokines, adhesion molecules and cytokines (ligand + receptor, x axis) in each EC subtype (y-axis). Dot size represents the percentage of cells in which the gene is detected. Color indicates the mean expression (in z-score).

(G-J) Flow cytometry quantification of $GrzB^+CD8^+$ cells (G and H), $PD1^+CD8^+$ cells (I), and T cell subsets (J) in PyMT tumors.

Data (n mice = 4-6) represent one of two independent experiments with similar results. Data are shown as mean ± SEM. Population distribution and median-quantile-min/max without outliers are shown in violin + boxplot (E). Krustal-Wallis test. $*$: $p < 0.05$.

Supplemental figure 3

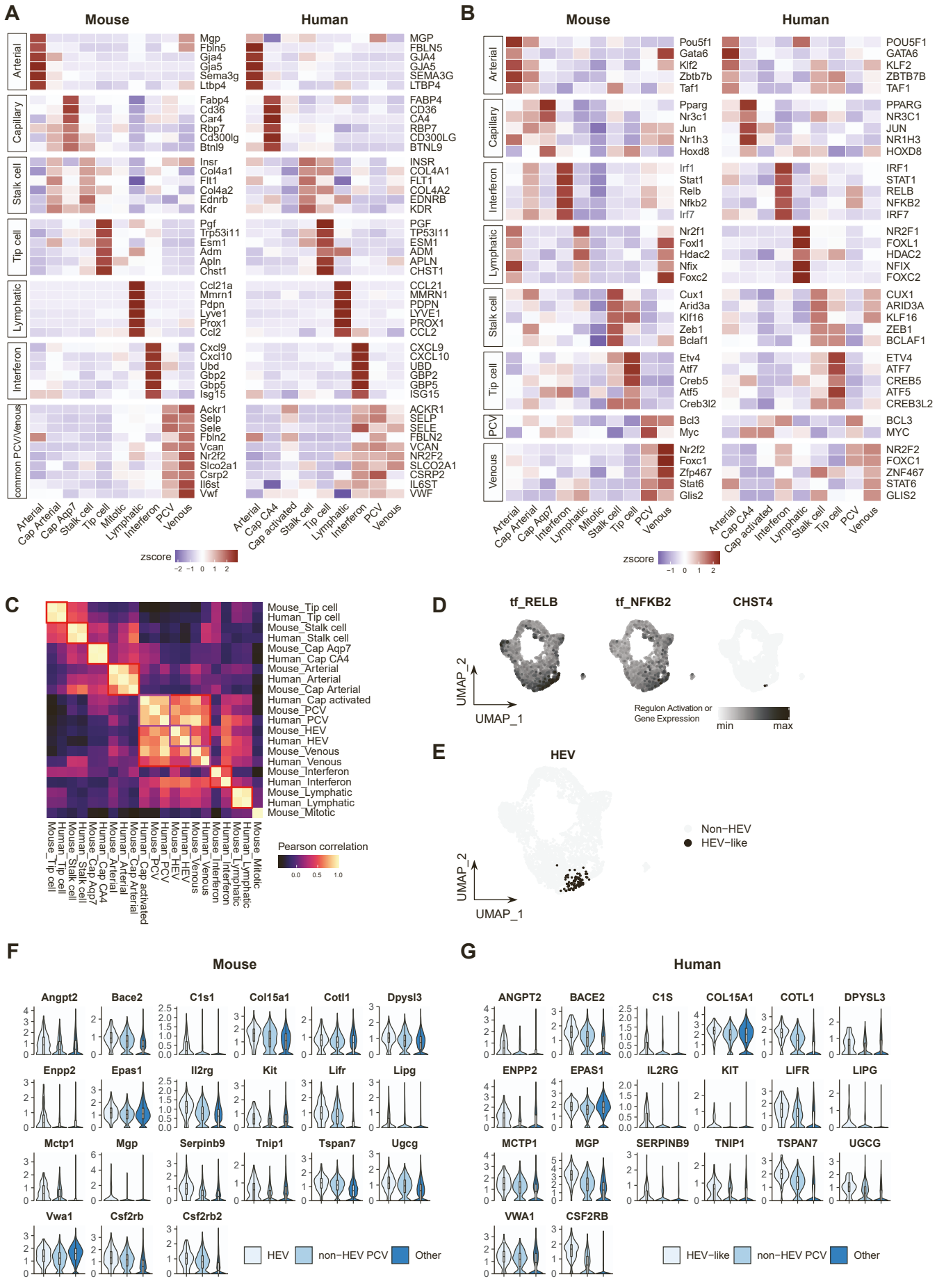

Figure S3. Characterization of the human tumor vasculature by scRNAseq, related to Figure 2.

(A and B) Conserved features (A) or regulons (B) of each EC subtype in mouse and human datasets. Homologous genes are shown in the same row.

(C) Pearson correlation of Harmony corrected principal components (PCs) exhibiting the similarity of each EC subtype in mouse and human.

(D and E) UMAP plots, colored by RELB/NFKB2 regulon activities predicted by SCENIC or expression of CHST4 (D), or *in silico* selected HEV cells (E).

(F and G) RNA expression levels of conserved TU-HEV features in mouse (F) and human (G) breast cancer datasets, comparing TU-HEVs, non-HEV PCVs and other ECs.

Population distribution and median-quantile-min/max without outliers are shown in violin + boxplot (F and G). Data are from one scRNA-seq experiment.

Supplemental figure 4

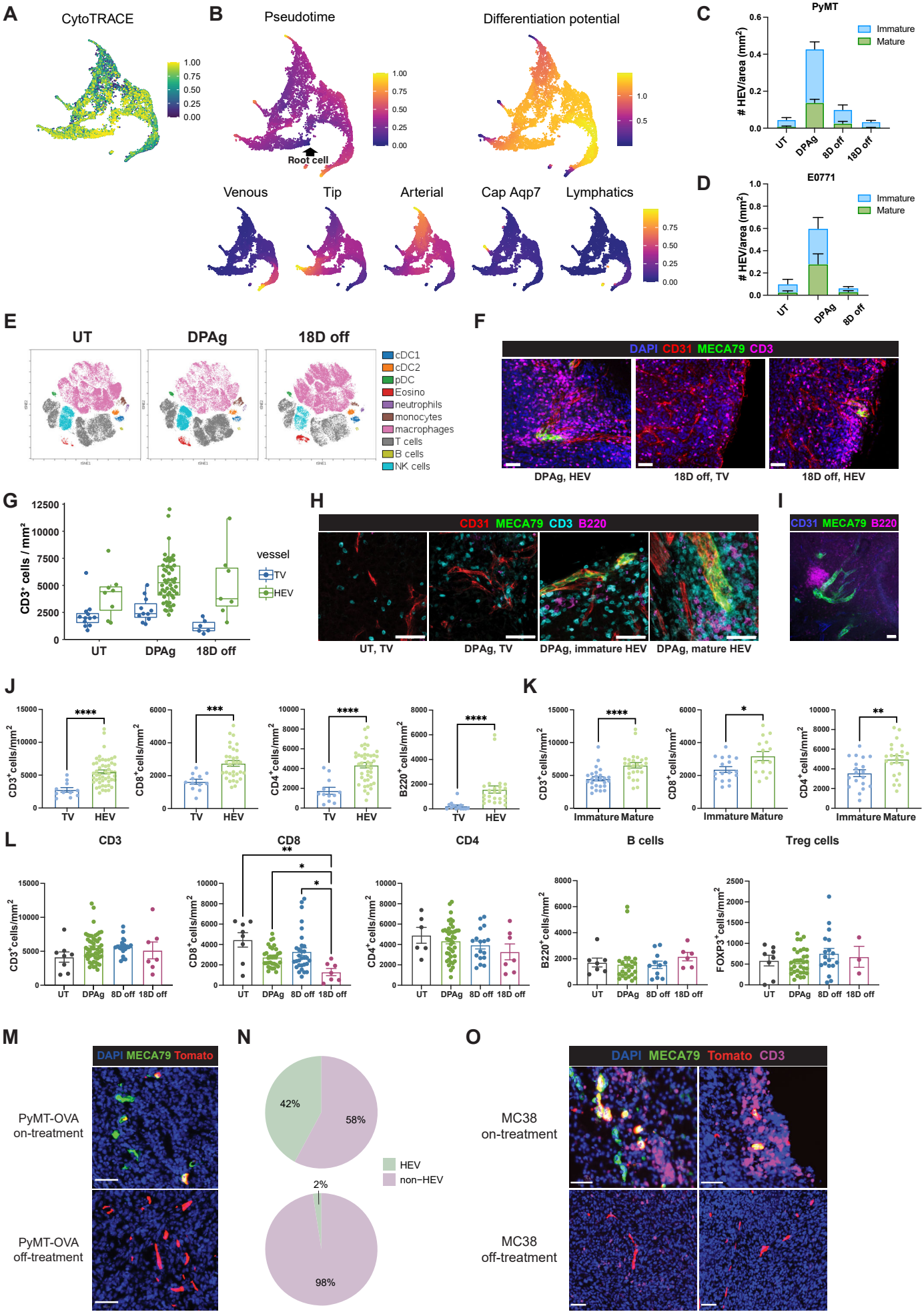

Figure S4. TU-EC metaplasia into TU-HEVs is dependent on immunotherapy-induced signals, related to Figure 3 and 4

(A and B) Differentiation potential predicted by CytoTRACE (A) or Palantir (B).

(C and D) Ratio of mature/immature HEV phenotypes of UT, DPAg or DPAg-stop PyMT (n tumors = 4-10) (C) and E0771 (n tumors = 11) (D) tumors by immunofluorescence tissue staining.

(E) Representative tSNE plots using the PyMT flow cytometry data.

(F) Representative pictures of DPAg HEV, 18D off tumor vessel (TV) and HEV in PyMT tumors, by confocal microscopy. Scale bar indicates 50 µm.

(G) Quantification of CD3 T cells 50 µm around TVs or HEVs from PyMT tumors by immunofluorescence tissue staining.

(H) Representative pictures of tumor vessels (TV) ($CD31^+MECA79^-$), immature/mature HEVs ($CD31^+MECA79^+$), B ($B220^+$) and T ($CD3^+$) lymphocytes in untreated (UT) and DPAg treated PyMT tumors. Scale bar indicates 50 µm.

(I) Representative picture of B cell cluster ($B220^+$) around HEV in PyMT tumor. Scale bar indicates 50 µm.

(J) Quantification of CD3 T cells (n = 11-51), CD8 T cells (n = 12-32), CD4 T cells (n = 12-42), and B cells (n = 13-24) 50 µm around HEVs or TVs in DPAg-treated PyMT tumors by immunofluorescent tissue staining.

(K) Quantification of CD3 T cells (n = 25-26), CD4 T cells (n = 19-23), and CD8 T cells (n = 15-17) 50 µm around mature HEVs and immature HEVs in DPAg-treated PyMT tumors by immunofluorescence tissue staining.

(L) Quantification of CD3 T cells (n = 7-51), CD8 T cells (n = 7-32), CD4 T cells (n = 6-42), B cells (n = 6-24), and Treg cells (n = 3-32) 50 µm around HEVs from PyMT tumors by immunofluorescence tissue staining.

(M and N) Representative images of PyMT-OVA tumors from Chst4-tdT reporter mice upon DCAg treatment (treatment ON) or after treatment cessation (treatment OFF) (M) and quantification of percentage of $dtTomato^+$ vessels that are $MECA79^+$ (HEV) or $MECA79^-$ (non-HEV) during treatment ON or treatment OFF (n tumors = 2). Scale bars indicate 50 µm.

(O) Representative images of CD3 T cells around $MECA79^+$ or $MECA79^-dtTomato^+$ structures in MC38 tumors from Chst4-tdT reporter mice upon CAg treatment (treatment ON) or after treatment cessation (treatment OFF). Scale bars indicate 50 µm.

The mean ± SEM are shown in bar plots (C, D, and J-L) and median-quantile-min/max without outliers are shown in boxplot (G). Mann-Whitney test (J and K). Krustal-Wallis test (L). $*$: $p < 0.05$; $**$: $p < 0.01$; $***$: $p < 0.001$; $****$: $p < 0.0001$. Data are pooled from at least two independent experiments (C, D, and J-L) or one experiment (M-O).

Supplemental figure 5

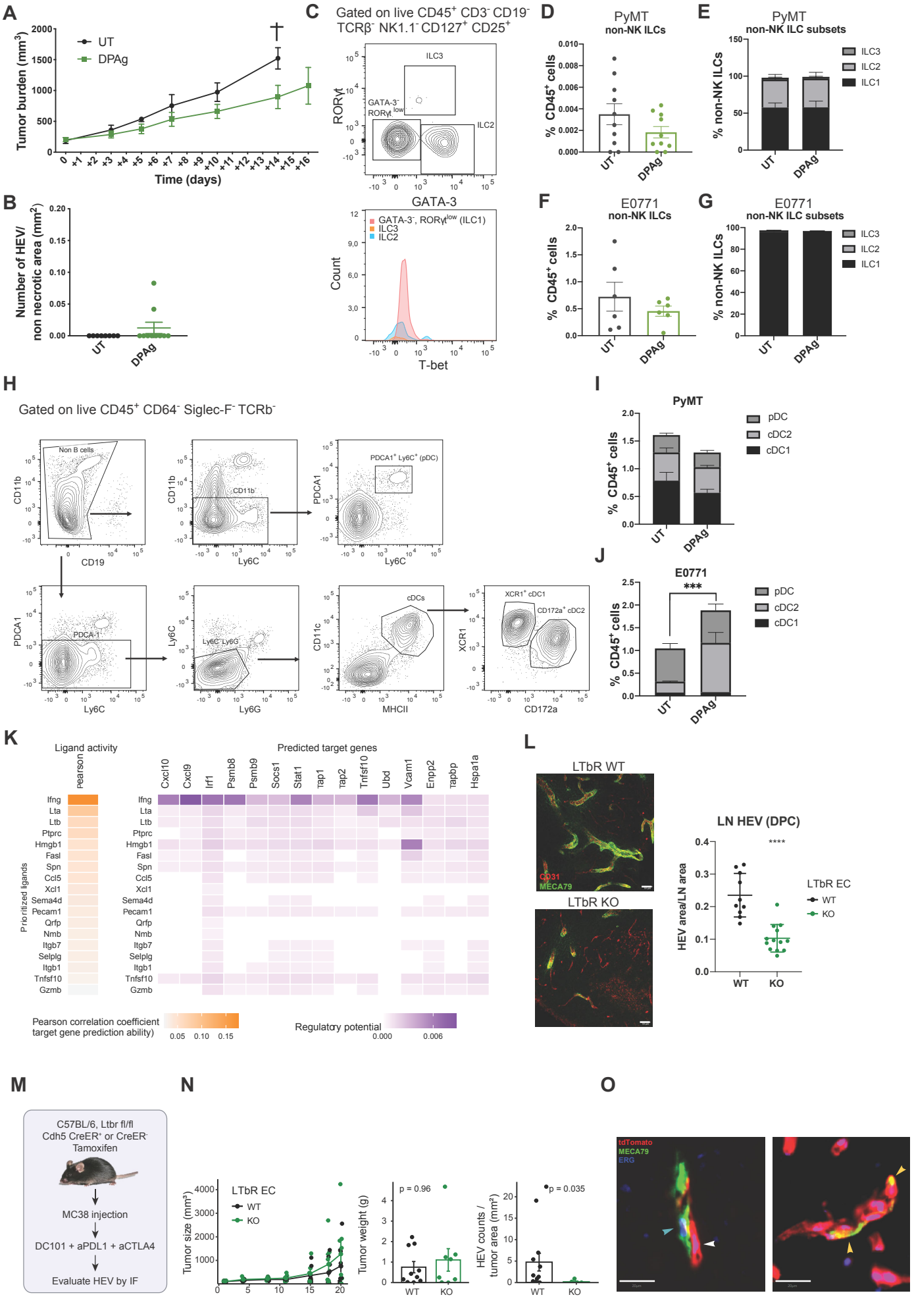

Figure S5. CD8 T-cells and NK cells induce immunotherapy-dependent HEV formation via the LT/LTβR axis, related to Figure 5

(A and B) Tumor growth curve (n = 7-9) (A) and HEV density (n tumors = 8-10) (B) of UT or DPAg treated PyMT-bearing Rag1 KO mice.

(C) Flow cytometry gating strategy for intratumoral non-NK ILC1, ILC2 and ILC3 based on the expression of Tbet (ILC1), Gata3 (ILC2) and Rorγt (ILC3) in $CD19^{-}CD3^{-}TCR^{-}NK1.1^{-}CD25^{+}$ $CD127^{+}$ cells.

(D-G) Flow cytometry quantification of non-NK ILCs in PyMT (n = 10) (D) and E0771 (n = 6) (F) and of each non-NK ILC subset in PyMT (n = 10) (E) or E0771 (n = 6) (G) tumors.

(H-J) Gating strategy for intratumoral $XCR1^{+}$ cDC1s, $CD172a^{+}$ cDC2s and $PDCA1^{+}$ pDCs by flow cytometry (H) and quantification of each DC subset in UT or DPAg treated PyMT (n = 10) (I) or E0771 (n = 6) (J) tumors.

(K) NicheNet predicts potential ligands secreted by T/NK cell components, which regulate EC phenotype after DPAg treatment.

(L) Representative images (left) and quantification (right) of LN-HEVs from PyMT-OVA-bearing LTβR wt (Cre^{-}) and LTβR KO (Cre^{+}) mice. Scale bars indicate 50 μm.

(M and N) Experimental design (M), tumor growth curves, final tumor weights, and HEV quantifications by immunofluorescence tissue staining (N) of MC38-bearing $LT\beta R^{ECKO}$ mice, treated by DC101 + anti-PD-L1 + anti-CTLA-4.

(O) Representative images of $MECA79^{+}$ cells that arise from either tdT^{-} (LTβR wt, lightblue arrow) or tdT^{+} (LTβR KO, yellow arrow) tumor vessels. White arrow indicates tdT^{+} ECs. Scale bars indicate 20 μm.

Data are shown as mean ± SEM. Statistics were assessed by Mann-Whitney test (B, D, F, L, and N) or two-way ANOVA (A at d14, E, G, I, and J). The statistical analysis is referred to cDC2 (J). ∗: $p < 0.05$; ∗∗: $p < 0.01$; ∗∗∗: $p < 0.001$; ∗∗∗∗: $p < 0.0001$. Data in D-G, I, and J are pooled from at least two independent experiments. Data from N derived from one experiment with 8-10 mice each arm.

Supplemental figure 6

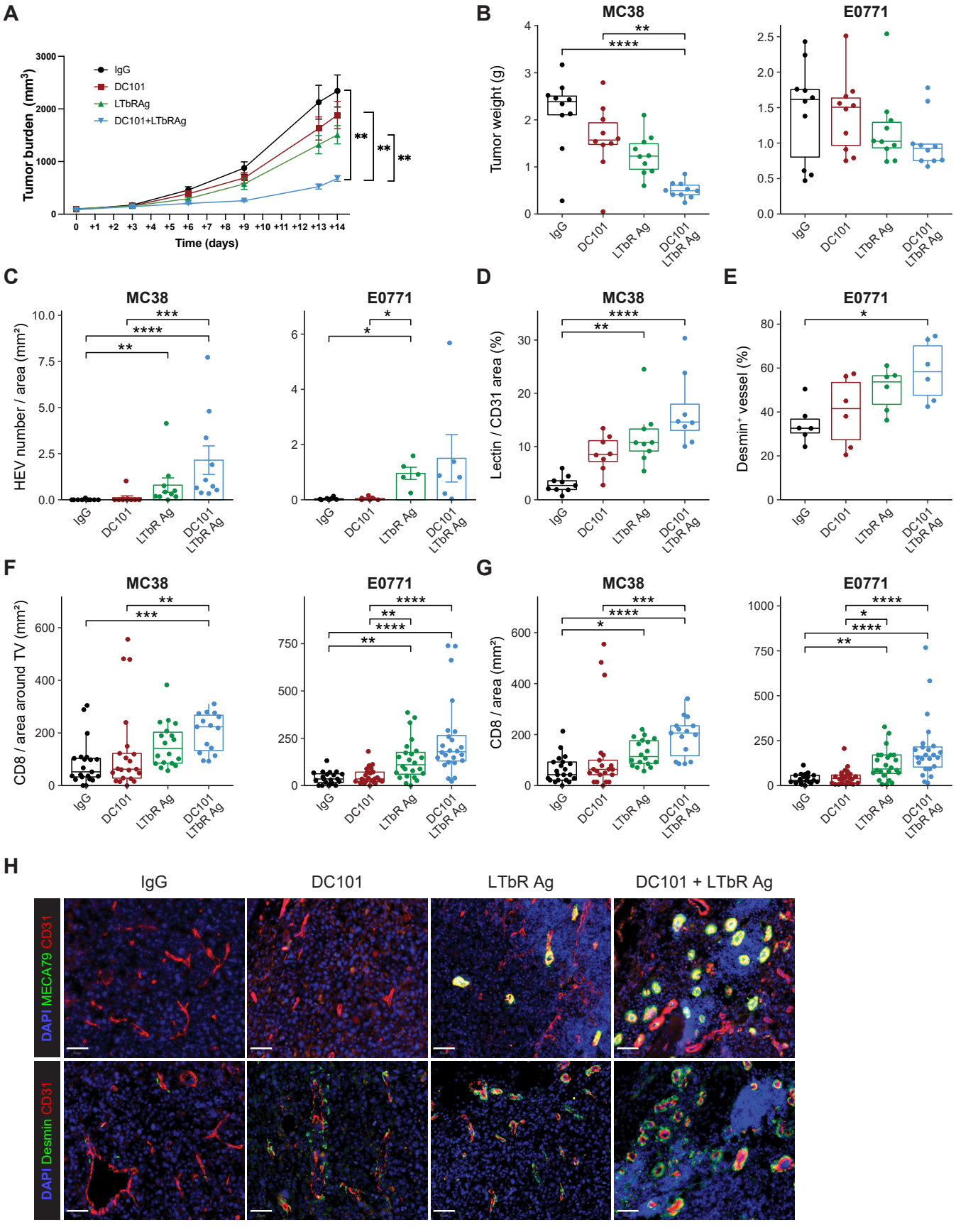

Figure S6. TU-HEV inducing therapy shows superior efficacy in controlling tumor growth compared to the anti-antiangiogenic therapy, related to Figure 5

(A) Growth curve of MC38 tumors treatment as indicated (n tumors = 10).

(B) Tumor weight of MC38 and E0771 tumors treated as in A. Tumors were collected 2 weeks after treatment start (n tumors = 10).

(C, F, and G) HEV density (C) and CD8 quantification 50 µm around TV (F) or in a 20X field (G) by immunofluorescence tissue staining of MC38 and E0771 tumors. In C, each symbol represents one tumor. n MC38 = 5-10; n E0771 = 5-7. In F and G, each symbol represents one field. n MC38 = 15-21; n E0771 = 20-24. 5-7 tumors were analyzed by cohort

(D) Percentage of vessel area overlapping with Lectin area calculated by immunofluorescence tissue staining. Each symbol represents one section (n = 8-9). 3 tumors were analyzed by cohort.

(E) Percentage of vessels covered by $Desmin^+$ pericytes by immunofluorescence tissue staining. Each symbol represents a tumor (n = 6).

(H) Representative immunofluorescence tissue staining of E0771 tumor treated as indicated and stained with anti-MECA79 and anti-CD31 (upper) or anti-Desmin and anti-CD31 (lower). Scale bars indicate 50 µm.

The mean ± SEM are shown in A and C, and median-quantile-min/max without outliers are shown in boxplots (B, and D-G). Statistics were assessed by two-way ANOVA (A) or Krustal-Wallis (B-G). $*$: $p < 0.05$; $**$: $p < 0.01$; $***$: $p < 0.001$; $****$: $p < 0.0001$. Data derived from two experiments with n mice = 5 each cohort per experiment.

Supplemental figure 7

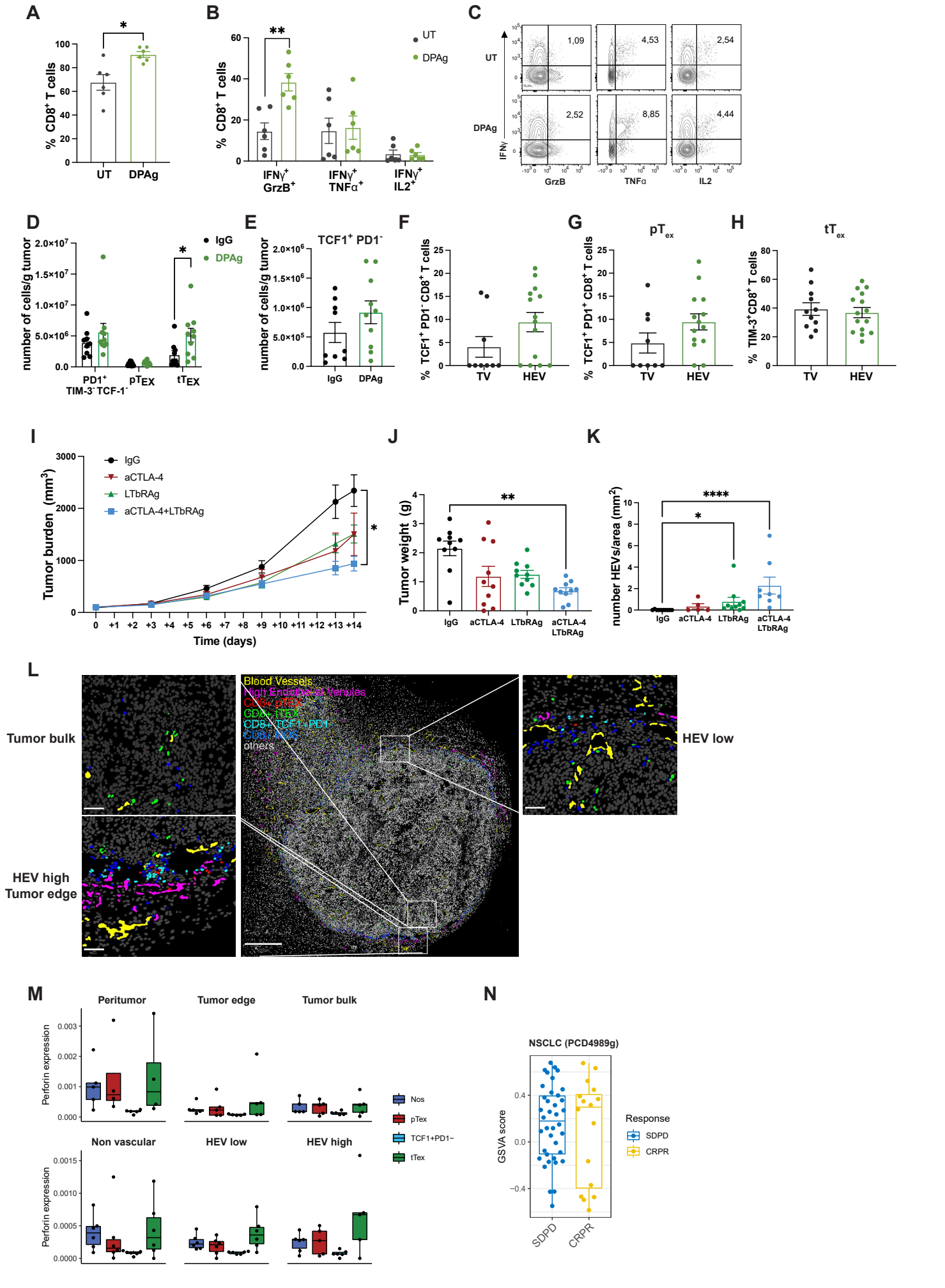

Figure S7. TU-HEVs generate TCF1$^+$ lymphocyte niches, related to Figure 6 and 7

(A and B) Flow cytometry quantification of PD1$^+$CD8$^+$ T cells (A) and of CD8$^+$ T cells co-expressing IFNγ-GrzB or IFNγ-TNFα or IFNγ-IL2 (B) in UT (n = 6) and DPAg (n = 6) treated E0771 tumors. The mean ± SEM are shown.

(C) Representative flow cytometry dot plots of IFNγ-GrzB or IFNγ-TNFα or IFNγ-IL2 CD8 T cells of UT and DPAg-treated PyMT tumors.

(D and E) Flow cytometry quantification of PD1$^+$ TCF1$^-$ TIM3$^-$ cells, pT_{EX} cells, tT_{EX} cells (D), and TCF1$^+$PD1$^-$ cells (E) in IgG (n = 9) and DPAg (n = 10) PyMT tumors.

(F-H) Quantification of TCF1$^+$PD1$^-$CD8$^+$ T cells (n = 9-14) (F), pT_{EX} (n = 9-14) (G), and tT_{EX} (n = 11-15) (H) 50 µm around HEVs or other tumor vessels from E0771 frozen sections.

(I-K) Growth curve (I), final weight (J), and HEV density by immunofluorescence tissue staining (K) of MC38 tumors treatment as indicated (n tumors = 10).

(L) Digital reconstruction of one representative MC38 tumor section stained with the MILAN multiplexing technique. Selected area depicts representative HEV low or HEV high area at tumor edge / bulk. CD8$^+$ pT_{EX} (red) are TCF1$^+$PD1$^+$TIM3$^-$; CD8$^+$ tT_{EX} (green) are TCF1$^-$PD1$^+$TIM3$^+$; CD8$^+$TCF1 (light blue) are TCF1$^+$PD1$^-$TIM3$^-$. All the remaining CD8$^+$ T cells are identified as CD8$^+$ NOS (Not Otherwise Specified) (blue). Scale bar indicates 500 µm. Scale bar in the selections indicates 100 µm.

(M) Boxplots indicating the perforin expression of CD8$^+$ T cells among the different subsets and in the different tumor areas in human breast cancer by the MILAN multiplexing technique (n tumors = 5-6).

(N) Boxplots showing the GSVA score of the HEV signature in non-small-cell lung carcinoma (NSCLC) patients before anti-PD-L1 therapy (Atezolizumab) from the PCD4989g study. PD=progression disease; SD=stable disease; PR= partial responder; CR=complete responder.

The mean ± SEM are shown in A, B, and D-K, and median-quantile-min/max without outliers are shown in boxplots (M and N). Statistics were assessed by Mann-Whitney test (A, B, D-H, and N), two-way ANOVA (I) or Krustal-Wallis (J and K). $*$: $p < 0.05$; $**$: $p < 0.01$; $***$: $p < 0.001$; $****$: $p < 0.0001$. Data are pooled from two independent experiments (A, B, and D-K). Human MILAN data are derived from five-six human untreated breast cancers (M).

Table S1: List of oligonucleotides used for RNAscope and list of primers used for qRT-PCR, related to STAR Methods.

REAGENT or RESOURCE	SOURCE	IDENTIFIER
Oligonucleotides		
RNAscope Probe Mm-C1s1	ACDBio	479961
RNAscope Probe Mm-Chst4	ACDBio	489931
RNAscope Probe Mm-Csf2rb	ACDBio	496431-C2
RNAscope Probe Mm-Glycam1	ACDBio	563741-C3
RNAscope Probe Mm-Il2rg	ACDBio	462211-C3
RNAscope Probe Mm-Lipg	ACDBio	492521-C3
RNAscope Probe Hs-CHST4	ACDBio	505181
RNAscope Probe Hs-CSF2RB	ACDBio	312441-C3
RNAscope Probe Hs-LIPG	ACDBio	487101-C3
RNAscope Probe Hs-IL2RG	ACDBio	412191-C4
RNAscope Probe Hs-C1S	ACDBio	508961-C4
RNAscope Probe Hs-FUT7	ACDBio	1061821-C1
RNAscope Probe Hs-PECAM1-O1	ACDBio	487381-C2
RNAscope 3-Plex positive control probe-Hs	ACDBio	320861
RNAscope 3-Plex positive control probe-Mm	ACDBio	320881
RNAscope 3-Plex negative control probe	ACDBio	320871
Primers		
mPerforin For: AAA AAC TCC CTA ATG AGA GAC GC	IDT	N/A
mPerforin Rev: ACA CGC CAG TCG TTA TTG ATA TT	IDT	N/A
mRpl19 For: CTG GAT GAG AAG GAT GAG GAT C	IDT	N/A
mRpl19 Rev: GGA TGT GCT CCA TGA GGA TG	IDT	N/A